AGU ADVANCING EARTH AND SPACE SCIENCES

AGU Advances

RESEARCH ARTICLE
10.1029/2025AV002247

Tidal River Flood Risk Highest During Intermediate Rather Than Peak River Discharge

Leicheng Guo[1], Adam T. Devlin[2], Ton Hoitink[3], Ian Townend[4], David A. Jay[5], Zheng Bing Wang[6,7], Chunyan Zhu[1], Hamed R. Moftakhari[8,9], Qing He[1], Fan Xu[1], Yuanyang Wan[10], Yuan Xu[1], and Weiming Xie[1]

[1]State Key Laboratory of Estuarine and Coastal Research, East China Normal University, Shanghai, China, [2]School of Ocean and Earth Science and Technology, University of Hawaii at Mānoa, Honolulu, HI, USA, [3]Department of Environmental Sciences, Wageningen University, Wageningen, the Netherlands, [4]School of Ocean and Earth Sciences, University of Southampton, Southampton, UK, [5]Department of Civil and Environmental Engineering, Portland State University, Portland, OR, USA, [6]Civil Engineering and Geosciences Faculty, Delft University of Technology, Delft, the Netherlands, [7]Deltares, Delft, the Netherlands, [8]Center for Complex Hydrosystems Research, The University of Alabama, Tuscaloosa, AL, USA, [9]Department of Civil, Construction and Environmental Engineering, The University of Alabama, Tuscaloosa, AL, USA, [10]Shanghai Estuary and Coastal Research Center, Shanghai, China

Peer Review The peer review history for this article is available as a PDF in the Supporting Information.

Key Points:

- Peak water levels (PWLs) in tidal rivers are highest under intermediate river discharge when subharmonic amplitudes culminate
- PWLs occur during the falling limb of discharge curves because hysteresis in river stage-discharge relation persists in tidal rivers
- Sediment depletion and channel deepening affect tidal river water level extremes, explaining the record-breaking Yangtze flood in 2020

Supporting Information:

Supporting Information may be found in the online version of this article.

Correspondence to:

C. Zhu,
cyzhu@sklec.ecnu.edu.cn

Citation:

Guo, L., Devlin, A. T., Hoitink, T., Townend, I., Jay, D. A., Wang, Z. B., et al. (2026). Tidal river flood risk highest during intermediate rather than peak river discharge. *AGU Advances*, *7*, e2025AV002247. https://doi.org/10.1029/2025AV002247

Received 12 DEC 2025
Accepted 6 JUN 2026

Author Contributions:

Conceptualization: Leicheng Guo, Adam T. Devlin, Ton Hoitink, Ian Townend, David A. Jay, Zheng Bing Wang, Chunyan Zhu
Data curation: Chunyan Zhu, Yuanyang Wan
Formal analysis: Leicheng Guo, Ton Hoitink, Chunyan Zhu, Qing He, Weiming Xie
Funding acquisition: Qing He

Abstract Tidal rivers are defined as the tide-influenced, salinity-free inland reaches of estuaries. Understanding the occurrence of peak water levels (PWLs) is critical for flood risk management, yet the timing and magnitude of PWLs in tidal rivers have been little studied. We address this gap by investigating PWLs during two catastrophic floods (1954 and 2020) in the tidal Yangtze River, which reveals that PWLs are higher during perigean spring tides under intermediate discharges following peak flow. Three factors modulate the PWLs in tidal rivers: river-enhanced tidal damping, flow-elevation hysteresis that raises the falling flow limb of the hydrograph, and low-frequency subharmonics. The latter, arising from nonlinear river-tide interactions, are distinct in tidal rivers and culminate under intermediate river flow as a result of the balance between tidal energy dissipation and the spectral energy transfer to subharmonics. They elevate PWLs by up to 0.3 m during perigean spring tides in the Yangtze case and amplify compound flood risk. Channel degradation has reduced tidal damping compared with circumstances in the 1950s, resulting in larger tidal ranges and record-breaking PWLs during the 2020 flood despite a smaller peak discharge. We identify tidal rivers spanning over 3,380 km in worldwide estuaries and deltas, where prevalent subharmonics like MSf are up to 0.65 m in amplitude. Many of those experience even larger tidal amplification due to channel deepening, implying escalating flooding risk under sea-level rise and human impact. These findings underscore a need to include nonlinear river-tide interactions in flood risk assessment for river-coast transition zones.

Plain Language Summary Flood risk management is a global challenge under climate change. Mitigating flood risk requires a better understanding of the factors controlling peak water levels (PWLs). Knowledge of PWLs in tidal rivers, the tide-influenced freshwater reaches, is a understudied problem at the boundary between fluvial hydrology and coastal oceanography. We examine two major floods in the tidal Yangtze River and find that PWLs occur during intermediate discharges rather than peak flow. This is attributed to nonlinear river-tide interactions stimulating fortnightly and monthly oscillations that raise tidally-averaged water levels at perigean spring tides, when the moon is either new or full and closest to Earth, and results in higher water levels during the falling limb of a river discharge hydrograph. The fortnightly variations are particularly profound in tidal rivers and can elevate PWLs by up to 0.3 m during the largest spring tides. We also show that channel deepening due to sediment starvation has made tides larger, explaining the record-breaking PWLs during the 2020 flood in the Yangtze. Similar driving mechanisms of PWLs are worldwide at play in estuaries and deltas, including the Mekong and Amazon. Our findings about the timing and magnitude of PWLs in tidal rivers inform flood risk projection and management in worldwide river-coast transition zones.

1. Introduction

Flooding is a leading cause of socio-economic losses from natural hazards. Global financial losses and fatalities due to flooding exceeded $23 billion and 5,900 people per year, respectively, during 1980–2012 (Jongman et al., 2015), with economic losses reaching $105 billion in 2022, because of climate change and increased occurrence of extreme events (Ganguli & Merz, 2019; Tessler et al., 2015). Compound flooding, which is most

Investigation: Leicheng Guo, Chunyan Zhu
Methodology: Leicheng Guo, Adam T. Devlin, Ton Hoitink, Ian Townend, David A. Jay, Zheng Bing Wang, Chunyan Zhu, Hamed R. Moftakhari, Qing He, Fan Xu, Yuanyang Wan, Yuan Xu
Project administration: Qing He
Resources: Leicheng Guo
Supervision: Zheng Bing Wang, Qing He
Validation: Leicheng Guo
Writing – original draft: Leicheng Guo, Ton Hoitink, Ian Townend, David A. Jay, Zheng Bing Wang, Chunyan Zhu, Qing He, Fan Xu, Yuan Xu, Weiming Xie
Writing – review & editing: Leicheng Guo, Adam T. Devlin, Ton Hoitink, Ian Townend, David A. Jay, Zheng Bing Wang, Chunyan Zhu, Hamed R. Moftakhari, Qing He, Fan Xu, Yuanyang Wan, Yuan Xu, Weiming Xie

Table 1
Characterization of Fluvial Rivers, Tidal Rivers, Tidal Estuaries, and Open Coasts in the River-Delta-Ocean Continuum in Terms of Geometric and Physiochemical Attributes

		Estuary and delta		
	River	Tidal river	Tidal estuary	Open coast
Channel depth	Uniform	Uniform or seaward increase	Uniform or seaward decrease	–
Channel width	Uniform	Uniform	Seaward increase (convergence)	–
Sinuosity	Low-moderate	Moderate-high	Low	–
Water salinity	Freshwater	Freshwater	Brackish	Saline
Tidal currents	Unidirectional	Unidirectional	Bi-directional	Rotating
Subtidal signal	Limited	Significant	Little	Limited
Wave influence	Limited	Limited	Limited-substantial	Substantial
Storm surge	Limited	Limited	Moderate	Substantial
SLR impact	Limited	Little-substantial	Substantial	Substantial
Flood drivers	Concentrated rainfall, high river discharge	High river discharge, high tide associated with spring tide, storm surge	High tide, storm surge, SLR	Concentrated rainfall, high tide, high waves, storm surge, SLR
Flood event examples	Floods in the middle-lower Yangtze River in 1954 (Xia & Chen, 2021)	The flood along the tidal Yangtze River in July 2020 (this study)	Hurricane Sandy hit New York in 2012 (Wahl et al., 2015)	Hurricane Harvey hit Texas in 2017 (Valle-Levinson et al., 2020)

likely to occur when high river discharge coincides with storm surges and spring tides, has gained progressively more attention over the past decades (Moftakhari et al., 2017, 2024; Wahl et al., 2015).

Tidal rivers are an inland reach of the river-to-coast transition zones; their landward end is the tidal wave limit, and seaward end is the location where fortnightly constituents like MSf become large enough to exert more influence on water level extremes (Guo et al., 2015; Hoitink & Jay, 2016; Sassi & Hoitink, 2013). Tidal rivers differ from fluvial systems in that they are affected by tides, and also differ from tidal estuaries because they are more landward in location, free from saltwater influence, and have distinctive tidal dynamics (Table 1). As the critical land-ocean transition zones, tidal rivers exhibit hydrological and morphological dynamics distinct from those of fluvial rivers and from the coast (Dalrymple & Choi, 2007; Gugliotta & Saito, 2019; Hoitink et al., 2017; Hoitink & Jay, 2016). Tidal rivers are characterized by a less convergent channel planform geometry, tidally variable but usually unidirectional (downstream) currents, and a combination of fluvial and tidal controls on total water levels (Table 1). Although tidal rivers are relatively inland in location, they are still surrounded by vast low-lying and densely populated floodplains susceptible to flood hazards related to large river discharges and high tides (Helaire et al., 2020).

Understanding the magnitude, timing, and drivers of PWLs is crucial for flood management. Existing studies of tidal dynamics in estuaries have documented the impacts of low-frequency tides in elevating tidally-averaged water levels, that is, subtidal water levels, during spring tides. In particular, the fortnightly constituent MSf, a pseudo-constituent with a period of 14.77 days, leads to higher high water during spring tides and possibly lower low water during neap tides (Elahi et al., 2020; Gallo & Vinzon, 2005; Godin, 1999; Guo et al., 2015; LeBlond, 1979; Losada et al., 2017; Sassi & Hoitink, 2013). The MSf tide arises as a forced signal in shallow estuarine waters because of the nonlinear river-tidal interactions such as between the astronomical M_2 and S_2 tides, satisfying the frequency relationship $\varphi_{MSf} = \varphi_{M2} - \varphi_{S2}$ (φ is tidal frequency) (Guo et al., 2020; LeBlond, 1979; Sassi & Hoitink, 2013; Wang et al., 1999). A similar effect is detected for the monthly constituent Mm with a period of 27.55 days that is generated from M_2-N_2 interactions, which satisfies $\varphi_{Mm} = \varphi_{M2} - \varphi_{N2}$. Mm causes higher subtidal water levels during perigean tides than apogean tides.

The MSf and Mm subharmonics are typically phase-locked with the spring-neap and perigean-apogean tidal variations (Aubrey & Speer, 1985; Guo et al., 2020; Losada et al., 2017), leading to higher subtidal water levels during spring tides and perigean tides than during neap tides and apogean tides, respectively. Subtidal water levels are higher during spring tides and perigean tides because tidal current velocities and subtidal friction are then larger, which necessitates higher subtidal water levels and a larger streamwise pressure gradient to maintain the momentum balance than during neap tides and apogean tides (Guo et al., 2020; LeBlond, 1979; Sassi & Hoitink, 2013).

While the impact of river-tide-surge interactions on PWLs and floods have been studied in deltas and at open coasts (Du et al., 2024; Spicer et al., 2019), to the authors' knowledge, the impact of subtidal oscillations on the magnitude and timing of extreme tidal river flood events has not yet been defined. This relates in part to the fact that subtidal oscillations can be masked by irregular water level fluctuations associated with time-varying river discharges. Flood risk along tidal rivers is more complex than the risk associated with fluvial and coastal flooding because of the nonlinear river-tide interactions and consequent subharmonics. Little is known about the timing, spatial structure and severity of floods in tidal rivers, where signals of river discharge peaking and tidal wave extremes are mixed.

We address the knowledge gap by examining and comparing two extreme flood events, which occurred in 1954 and 2020 in the lower Yangtze River, where fatalities occurred in multiple regions of the river. We particularly focus on the tidal-river flooding under both high river discharge and strong tides. We will employ multiple methods to identify and isolate the impact of river flow, tides, and river-tide interactions on the total water levels and PWLs, including frequency and harmonic analyses, continuous wavelet transforms (CWT), and numerical modeling. Based on an in-depth examination of river discharge-tide interactions, we reveal how fortnightly and monthly subtidal oscillations can modulate both the magnitude and timing of PWLs in the tidal Yangtze river, and discuss the relevance for tidal rivers worldwide.

2. Materials and Methods

2.1. Yangtze Estuary

China is particularly vulnerable to devastating floods, with an average of 20 large floods per year and a total of 900 million people affected between 2000 and 2019 (UNDRR, 2020). Many floods have occurred in the middle-lower Yangtze River (Figure 1), including catastrophic flooding in 1954 and 1998 resulting in thousands of fatalities and billions in economic losses (Xia & Chen, 2021; Table 2). The Yangtze Delta is considered to be one of the global large deltas most highly susceptible to flood hazards (Balica et al., 2012; Tessler et al., 2015), due to its low-lying relief, large population (>200 million) and properties exposed to flood risk from high river discharge, large tides, and storm surges. The recorded maximal river discharge is up to 92,600 m^3/s, while the maximal tidal range is approximately 5.9 m (Guo et al., 2015). The tides in the Yangtze Estuary have a predominantly semi-diurnal regime, with M_2 being the most important constituent, followed by S_2, K_1 and O_1, and a form number, the $(O_1 + K_1)/(M_2 + S_2)$ amplitude ratio, between 0.2 and 0.3 at the mouth.

To mitigate flood risk in the Yangtze, the Three Gorges Dam (TGD) was constructed 1,100 km upstream of the delta, which has been operational since 2003. Despite this, another severe flood occurred in July 2020 in the middle-lower Yangtze River (see Figure S3 in Supporting Information S1), owing to strong rainfall concentrated in the basin downstream of the TGD, related to an extreme of the Indian Ocean Dipole (Wei et al., 2020; Z. Zhou et al., 2021). This event displaced 45.5 million people, caused the loss of 219 lives, and incurred direct economic losses of some ¥179 billion (Wei et al., 2020; Table 2).

A preliminary look at the data during the 2020 flood suggested that the PWLs in the tidal Yangtze River exceeded the historical maximum of 1954 by 0.2 m on average, whereas the peak flood discharge at Datong, near the tidal wave limit, was actually smaller, that is, 84,500 m^3/s in 2020 compared to 92,600 m^3/s in 1954 (Table 2). In addition, we note that the tidal river reaches between Datong and Jiangyin experienced higher PWLs than in 1954, whereas PWLs in the fluvial reaches upstream of Datong and in the seaward tidal estuary part seaward Jiangyin were not particularly higher (Figure 1). These observations give rise to critical questions as to why the PWLs in the tidal river only were record-breaking higher during the 2020 flood. The unusually high PWLs inspire us to further look into both events in 1954 and 2020 and lead to the hypothesis that subtidal water level variations and long-term tidal changes may play a role on the timing and magnitude of PWLs.

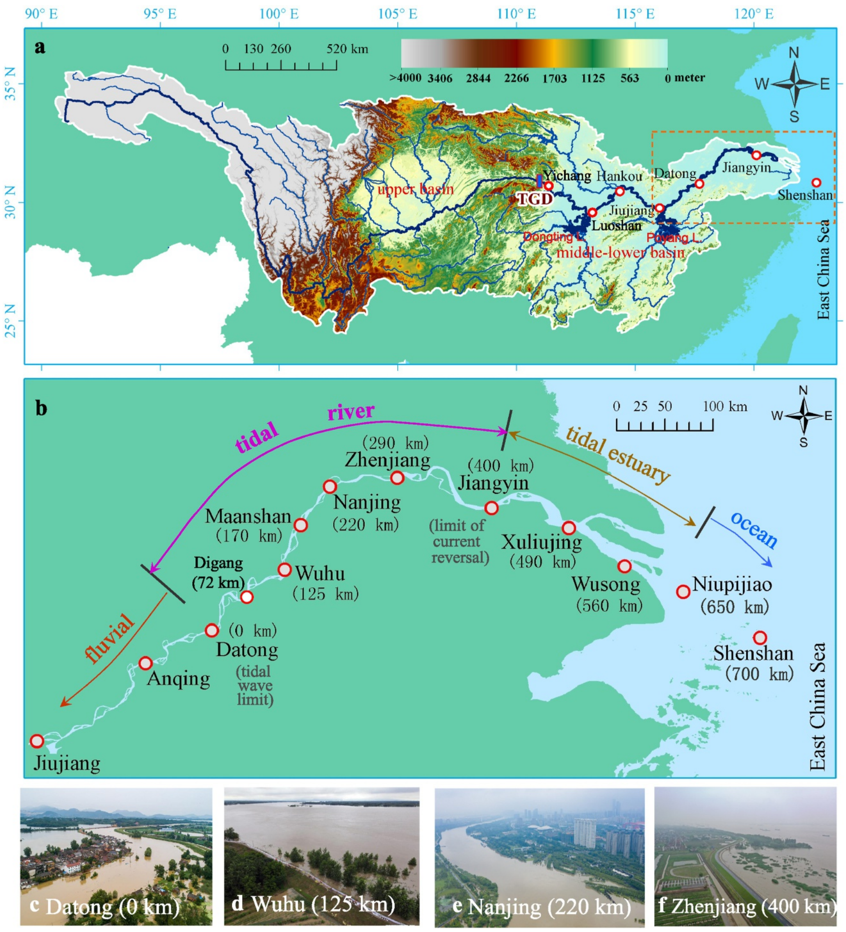

Figure 1. Maps of the Yangtze River basin and the delta region, and photographs capturing the extreme flooding along the tidal river in July 2020. (a) A Digital Elevation Model showcasing the topography of the Yangtze River basin. (b) An overview of the river flow gauges and tidal gauges in the lower Yangtze River. (c–f) Photographs illustrating the extent of flooding along the tidal river (sourced from www.people.com.cn and www.news.cn). TGD in panel (a) denotes the Three Gorges Dam. The numbers in the parentheses in panels (b–f) indicate the downstream distances from Datong, near the tidal wave limit, under medium-to-high river flow conditions. Note that the tidal wave limit and flow reversal limit migrate with river discharge, thus the length of tidal river adapts accordingly.

Table 2
Statistics of Four Extreme Flood Events in the Yangtze River and Resultant Casualties and Economic Losses

	Peak river discharge (m^3/s)			Peak water levels in the delta (m)					Flood hazards	
Year	Yichang	Hankou	Datong	Datong	Nanjing	Zhenjiang	Jiangyin	Wusong	Casualties	Economic losses[a]
1931	64,600	59,900	–	–	–	–	–	–	145,000	–
1954	66,800	75,900	**92,600**	16.64	**10.22**	**8.59**	6.70	5.12	33,000	10
1998	63,300	76,100	82,300	16.32	10.14	8.37	6.43	4.93	1,320	166
2020	50,850	61,220	**84,500**	16.24	**10.39**	**8.82**	6.40	4.52	219	179

Note. "–" indicates data are not available. Gauges are referred to Figure 1. The peak water levels are referenced to the Wusong Datum. The bold numbers highlight the historical extreme flood in 1954 and the recent 2020 flood during which peak water levels in the tidal river surpass the values in 1954. [a]Economic losses are presented in Chinese RMB (¥) in billion without considering currency value changes.

2.2. Data and Methods

We compiled river discharge data from the main river downstream of the TGD (https://www.cjh.com.cn) and tidal height data from 11 gauges across the Yangtze River delta for the periods of 1953–1954 and 2020–2021 (www.jsswj.com.cn; Guo, 2026). Rigorous quality checks of raw data to eliminate anomalies were undertaken, including checking data consistency, data gap, and datum corrections. All water levels were referenced to a common datum, that is, the low water level at Wusong.

To determine the drivers of PWLs and the contributions of river and tidal forcing, we combined frequency analyses and modeling techniques. First, we used low-pass and high-pass filters to separate tides and subtidal signals, based on a frequency threshold of 0.75–1.25 cycles per day. A low-pass filter is applied to the hourly water levels (the total water levels, h_m) to yield subtidal water levels (h_s). A high-pass filter outputs water level variations in the tidal frequency band (h_t) including contribution of diel astronomical tides, and high-frequency overtides and compound tides (e.g., M_4 and MS_4). The subtidal water levels primarily reflect contributions from the river flow (h_r) and possible low-frequency subharmonics (h_{so}), such as fortnightly and monthly variations related to MSf and Mm constituents, respectively. Subtidal oscillations are discerned as the disparities between the daily-averaged and fortnightly-averaged water levels.

The tidal range is computed at hourly intervals from the water level time series using a high-pass filter that eliminates subtidal variations. The data are then interpolated into 6-min intervals, and tidal ranges are defined by the differences between minimum and maximum heights using a 27-hr moving window (Matte et al., 2013). Harmonic analysis is used to determine amplitudes of individual tidal constituents like M_2, S_2, and MSf, utilizing 1-to-3-month data intervals during dry (Jan.-Mar.) and wet (Jun.-Aug.) seasons when river discharge fluctuations are minimal (Pawlowicz et al., 2002). CWT are utilized to generate frequency spectra of water levels, which served as a valuable complementary approach to unveil non-stationary tidal variations. Further details of the CWT method can be found in Grinsted et al. (2004) and Guo et al. (2015).

A numerical tidal model based on Delft3D software is employed to better understand the dynamics of river-tide interactions and their impact on the generation of subharmonics. The schematized model spans 1,000 km in length and adopts a convergent planform, with the width varying from 1 km on the river side to 10 km on the coastal side (see Figure S1 in Supporting Information S1), replicating a long tidal channel, similar to the lower Yangtze River in terms of length, width convergence, and depth. Constant river discharge of 0, 10,000, 30,000, 60,000 and 90,000 m^3/s, and three major semi-diurnal astronomical tidal constituents (M_2, S_2, and N_2) are prescribed to enable internal generation of MSf and Mm tides, while the diurnal tides are excluded, considering that the diurnal tides do not contribute to internal generation of MSf and Mm. An equilibrium bed profile obtained from long-term morphodynamic simulations is utilized in the tidal simulations to minimize disjunction between boundary forcing conditions and channel morphology. Although the model is simplified, it captures the nonlinear tidal dynamics and functions as a virtual laboratory, enabling straightforward examination of spatial-temporal variations of subtidal signals and PWLs, independent from the complexities associated with non-stationary river discharge and irregular geometry. Further details of the model are provided in Guo et al. (2020) and in Supporting Information S1.

3. Results

3.1. PWLs Along the Tidal River

We first examined the tidal data to clarify the variability of PWLs. The disastrous 2020 flood impacts in the tidal Yangtze River are illustrated in Figures 1c–1f. Water levels above critical flood hazard thresholds persisted for months, due to very high river flow (Xia & Chen, 2021). A closer examination of water level data reveals, however, important water level variations related to tidal processes and tidal-fluvial interactions that are not considered in typical flood management scenarios.

PWLs along the tidal river during the 2020 flood set new records and exceeded the previous highest levels recorded in 1954, whereas the peak discharge at Datong was 8,100 m^3/s lower in 2020 than in 1954. Specifically, the PWLs in 2020 were 0.21 m, 0.17 m, and 0.23 m higher at Ma'anshan (km-170), Nanjing (km-220), and Zhenjiang (km-290), respectively (Table 3).

Table 3

Peak Water Levels (PWLs) in the Tidal Yangtze River During the 2020 Flood and the Drivers, Including Flooding Warning Levels (A), Extreme Water Levels in 1954 (B); Extreme Water Levels in 2020 (C1 and C2); Tidal Ranges (D1 and D2); Detided Water Levels (E1 and E2); and Their Differences Between the Perigean Spring Tide on 20–21 July and the Apogean Neap Tide on 13–14 July 2020

		Flood warning level (m)	PWL in 1954 (m)	13–14 July 2020 (apogean neap tide)			21–22 July 2020 (perigean spring tide)			The differences between apogean neap tide and perigean spring tide (m)			Contribution of subtidal oscillation to extra PWL
				PWL (m)	Tidal range (m)	Detided water levels (m)	PWL (m)	Tidal range (m)	Detided water levels (m)				
		A	B	C1	D1	E1	C2	D2	E2	C2-C1	(D2-D1)/2	E2-E1	(E2-E1)/(C2-C1)
Fluvial river	Max. Q (m^3/s)		**92,600**		**84,500**			**76,000**					
	Datong	14.40	16.64	16.24	0.05	16.13	16.03	0.05	16.01	−0.21	0.00	−0.12	–
Tidal river	Wuhu	11.20	12.87	**12.60**	0.08	12.58	**12.76**	0.16	12.66	**0.16**	0.04	**0.08**	**52%**
	Ma'anshan	10.00	**11.46**	**11.42**	0.11	11.36	**11.67**	0.24	11.51	**0.25**	0.07	**0.15**	**58%**
	Nanjing	8.70	**10.22**	**10.09**	0.15	10.00	**10.39**	0.38	10.18	**0.30**	0.11	**0.18**	**60%**
	Zhenjiang	7.00	**8.59**	**8.26**	0.27	8.14	**8.82**	0.80	8.36	**0.56**	0.27	**0.22**	**40%**
Tidal estuary	Jiangyin	5.90	7.22	5.09	0.82	4.59	6.39	2.52	4.91	1.30	0.85	0.31	24%
	Xuliujing	5.10	6.75	4.12	1.11	3.38	5.45	2.99	3.68	1.33	0.94	0.30	23%
	Wusong	4.80	5.74	3.42	1.37	2.54	4.52	3.14	2.75	1.10	0.88	0.21	19%
Coastal ocean	Shenshan	3.65	–	2.70	1.57	1.68	3.56	3.75	1.67	0.86	1.09	−0.01	–

Note. The maximum river discharge (Q) is recorded at Datong. The bold numbers indicate the situation with record-breaking PWLs occurred during perigean spring tide. The water levels are referenced to the Wusong Datum.

The record-breaking PWLs only occurred along the tidal river between Datong and Jiangyin, and not in the upstream fluvial river or in the seaward tidal estuary. In addition, PWLs did not coincide with the discharge maximum on July 13–14, but occurred approximately one week later, on July 20–21, during a spring tide when the river discharge had receded to 76,000 m^3/s (Figure 2c). At that time, the PWLs were 0.30 and 0.56 m higher on July 20–21 compared to July 13–14 at Nanjing and Zhenjiang, respectively (Table 3).

A revisit of historical data during the 1954 floods shows a similar time lag effect. The peak discharge of 92,600 m^3/s occurred during the apogean spring tide on August 1–2, 1954 (Figure 2b), while PWLs in the tidal river occurred during the subsequent perigean spring tide on August 15–16 (Figure 2d), coinciding with a river discharge decreased to 81,600 m^3/s. On August 15–16, the maximum tidal ranges were 0.44 and 0.50 m greater at Jiangyin and Wusong than two weeks earlier, respectively (Figure 2f). The subtidal water levels were 0.34 m higher at Jiangyin by mid-August (Figure 2d). Thus, PWLs occurred on August 1–2 in the fluvial river upstream of Datong, synchronized with the peak discharge, but appeared 2 weeks later in the tidal river (Figure 2d). The lagged occurrence of PWLs in the tidal river in 1954 was similar to the 2020 flood.

The identified 7–15 days time lag of the PWLs relative to the peak discharge during both floods cannot be explained by the downward propagation of river flood waves. The flood wave takes less than 2 days to propagate from Datong to Jiangyin, a distance of 400 km, if one assumes an indicative wave celerity of 1.5 times the flow velocity. Consequently, the magnitude and timing of PWLs in the tidal river during both events cannot be attributed to a simple summation of river and tidal influences and the downstream flood wave propagation. There is therefore a need to investigate other possible explanations.

3.2. Drivers of Tidal River PWLs

In this section, we identify drivers of the PWLs in the tidal river subject to study. There was no storm surge event during the flood periods of 2020. Furthermore, the tidally-averaged sea level did not show abrupt changes that could exacerbate flooding during spring tide, although the yearly-averaged mean sea levels increased over much longer time scales (Figure S4 in Supporting Information S1). The total water levels are a nonlinear composite of river and tidal impact (Figure 4d), with their energy dissipating in the seaward and landward directions,

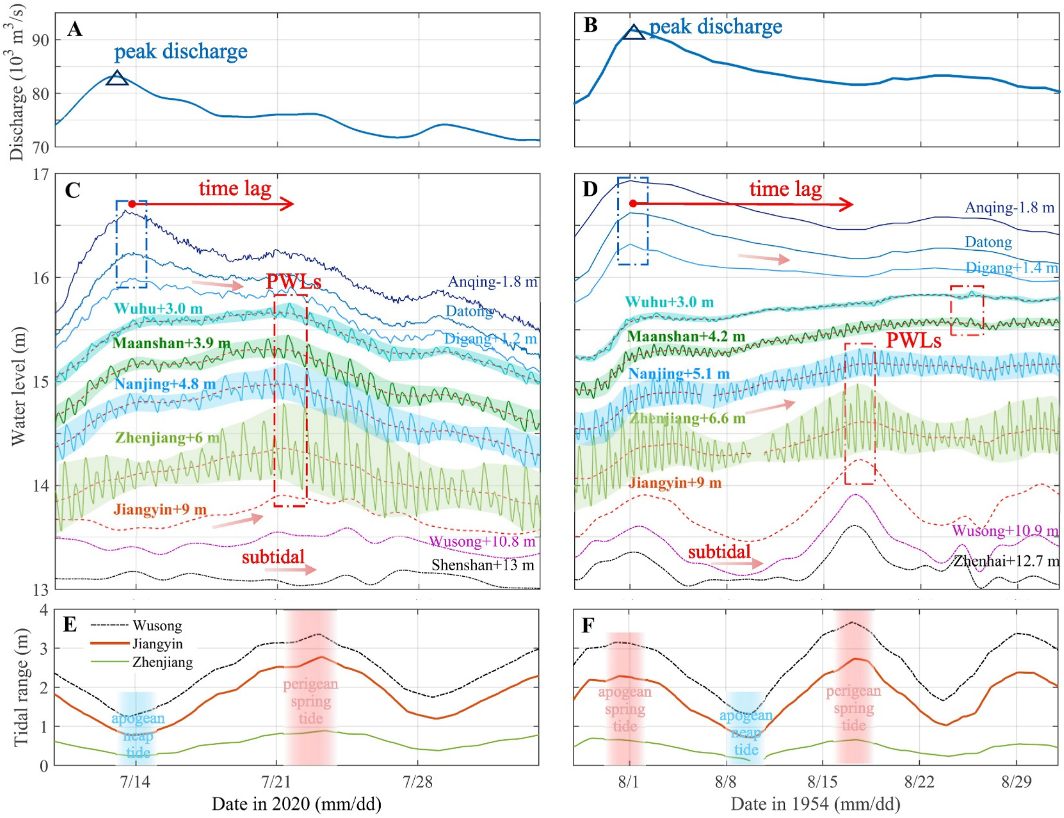

Figure 2. Comparative illustration of the magnitude and timing of Peak water levels (PWLs) in the river-delta continuum during the floods in July 2020 (left panels) and August 1954 (right panels). (a and b) River discharge at Datong. (c and d) Hourly water levels (solid lines) and daily-averaged water levels (dash lines) at multiple gauges in the reaches between Datong and Shenshan. (e and f) Daily tidal range variations at Wusong, Jiangyin, and Zhenjiang. The water levels in panels (c and d) are vertically offset for improved visualization, and the red rectangles indicate the period of PWLs. Only subtidal water levels are presented for Jiangyin, Wusong, and Shenshan in panels (c and d).

respectively. The primary determinants of PWLs in the tidal Yangtze River then hinge on the dynamics of river flow (Figure 4a), tides (Figure 4b), and their interactions (Figure 4c).

Increased river discharges elevate the tidally-averaged water levels throughout the tidal river (Figure 3). This results in significantly higher mean water levels under higher river discharge in the wet seasons than in the dry seasons, that is, a rise by 12 m when river discharge increased from 10,000 m^3/s to 80,000 m^3/s at Datong (Figure 4a). The river-induced subtidal water level rise decreases in magnitude in the seaward direction, and becomes much smaller downstream of Jiangyin (Figure 4a). Specifically, between July 1 and 14, 2020, river stage at Datong surged by 3.5 m as river discharge increased from 50,000 m^3/s to 84,500 m^3/s over a period of 13 days. Similarly, the subtidal water levels rose by 2.4 and 0.8 m at Nanjing and Jiangyin, respectively, suggesting pronounced fluvial impacts throughout the tidal river.

Tides induce additional water level variations around the mean values. Astronomical tides exhibit diurnal, semi-diurnal, or mixed diurnal cycles, and show changes in amplitudes at fortnightly, monthly, and interannual time scales after entering estuaries. Tidal waves are strongly damped within the Yangtze Estuary due to high river discharge and bed shear stress, leading to landward decreasing tidal ranges inland of Niupijiao (Figure 4b). Spring tides are damped at a larger rate than neap tides. River flow enhances tidal damping, particularly upstream of Jiangyin (Figure 4b), that is, reducing the spring tidal range by 1.10 m at Nanjing when the river discharge increases from 14,000 m^3/s to 75,000 m^3/s (Figure 5b). This river-enhanced tidal damping and reduction in tidal ranges tends to mitigate the river contribution in elevating the total water levels.

Tides affect PWLs by inducing higher water levels during perigean and spring tides. Maximum tidal ranges were 2.50 and 0.80 m at Jiangyin and Zhenjiang, respectively, during the perigean spring tide on July 20–21, which

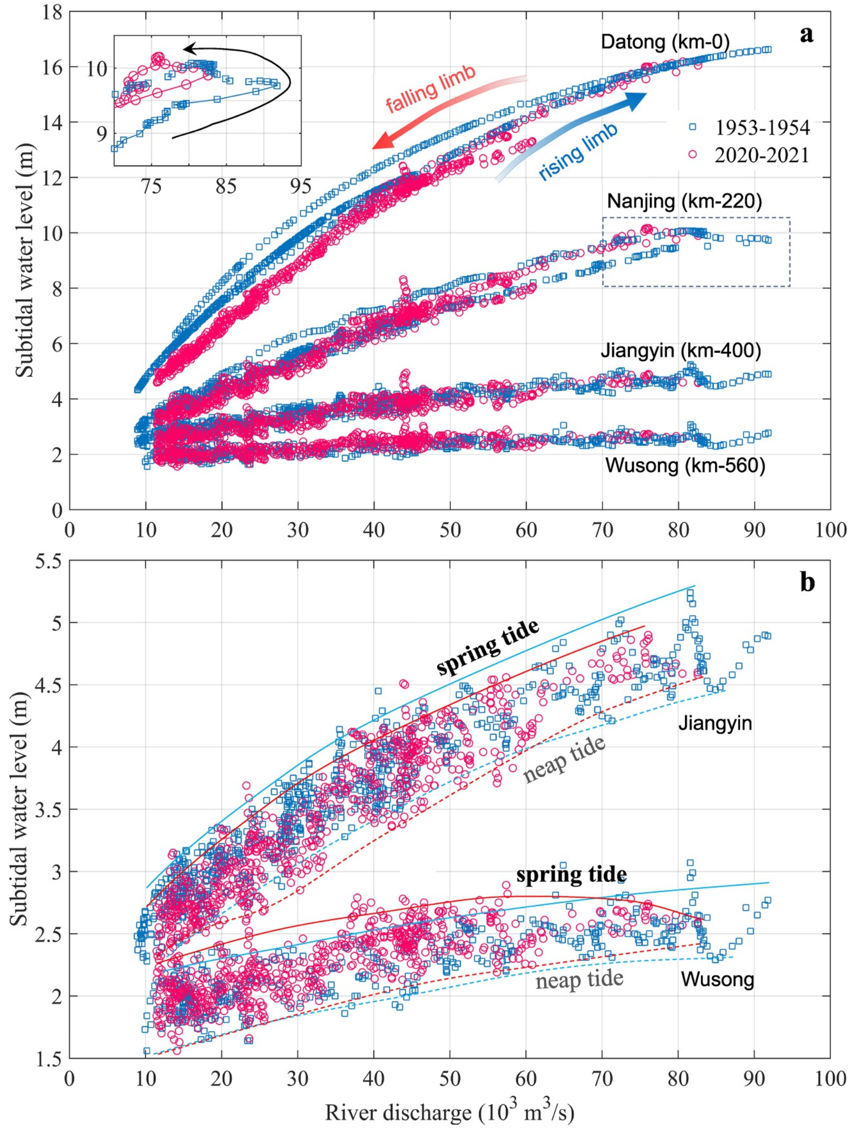

Figure 3. (a) Changes of subtidal water levels in the tidal Yangtze River, that is, at Datong (km-0), Nanjing (km-220), Jiangyin (km-400), and Wusong (km-560), with increasing river discharges at Datong, based on data in 1953–1954 (blue) and 2020–2021 (magenta). (b) Zoom-in of the changes at Jiangyin and Wusong. The small box in panel (a) shows the zoom-in of the high discharge condition at Nanjing. The solid and dashed lines in panel (b) indicate the envelops of the scattered dots at spring tides and neap tides, respectively.

were much larger than 0.85 and 0.20 m during the apogean neap tide on July 13–14 (Figure 2e). The greatest high waters in the high-pass filtered water levels from which the river impact was removed were 1.00 and 0.32 m higher on July 20–21, for the two stations. This suggests that larger tidal ranges during the perigean spring tides around July 20–21 partially explain the higher and lagged PWLs in the tidal river than a week earlier (Table 3).

In addition, the subtidal water levels exhibited variations out of phase with river discharge fluctuations. Following the river discharge reduction in the week after the peak (from 13 to 14 to 20–21 July), the subtidal water levels decreased by 0.12 m at Datong, at the river side of the tidal river, and exhibited minimal variations at Shenshan, at the sea side (Figure 2c). However, they continued to increase at all gauges along the tidal river, for example, by 0.22 m at Zhenjiang from July 13–14 to 20–21 (Figure 2c). This subtidal water level rise, which was inconsistent with the river discharge fall, contributed to the total water level increase over the week. To highlight its impact, we compared the differences between the total water levels and the subtidal water levels during July 13–14 and July 20-21, and estimated that the extra rise in subtidal water levels contributed 40%–60% of the augmented PWLs on

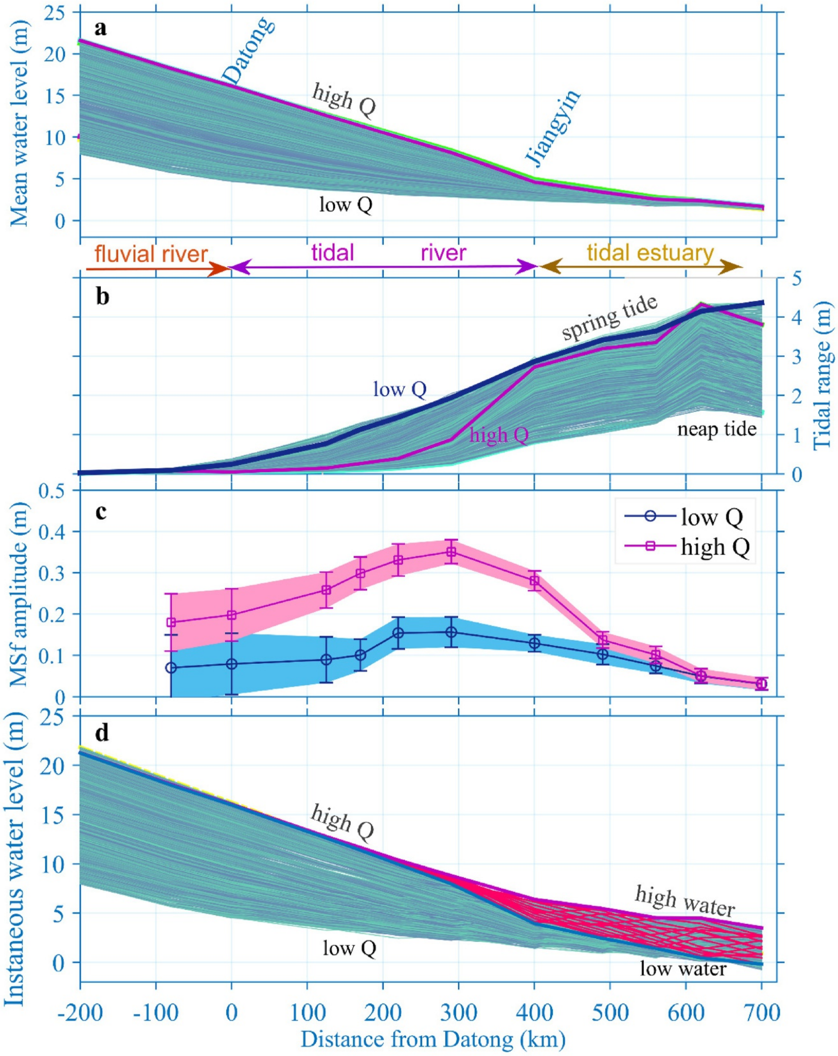

Figure 4. Longitudinal distribution of water levels and tidal properties in the lower Yangtze River during June and August 2020. (a) Detided water levels with tidal oscillations removed. (b) Daily tidal ranges. (c) Harmonically resolved MSf tidal amplitude under low (~11,000 m^3/s) and high (~70,000 m^3/s) river discharges. (d) Instantaneous water levels, that is, the total water levels, as the summed contribution of panels (a–c), for high river discharge (high Q) and low river discharge (low Q), during spring tide and neap tide. High water and low water conditions are highlighted (thick lines). The distance from Datong is defined as positive in the seaward direction and negative in the upstream direction.

20–21, compared to 13–14 July (Table 3). This analysis underscores the significance of subtidal water level variations in amplifying PWLs and modulating their timing.

To highlight the subtidal oscillations independent of variable river flow, we further employed a CWT to the time series of tidal height data. The CWT-resolved time-frequency spectra demonstrated landward dissipation of the diurnal and semi-diurnal tides (see Figure S5 in Supporting Information S1). Moreover, the CWT spectrums also illustrated internal generation of fortnightly signals in the tidal Yangtze River (e.g., at Jiangyin), while the subtidal signals were insignificant near the coast (e.g., at Shenshan; see Figure S5 in Supporting Information S1). This CWT analysis also indicated tidal wave spectra evolution in the landward direction, and confirmed landward attenuation of the diurnal and semi-diurnal astronomical tides and energy gain at the sub-frequency bands.

3.3. Impact of Long-Term Tidal Changes

To explain the record-breaking PWLs in 2020, we explored possible long-term changes by comparing the tidal data for the 1954 flood with the 2020 event. Both years had average amplitudes in terms of the 18.6-year nodal

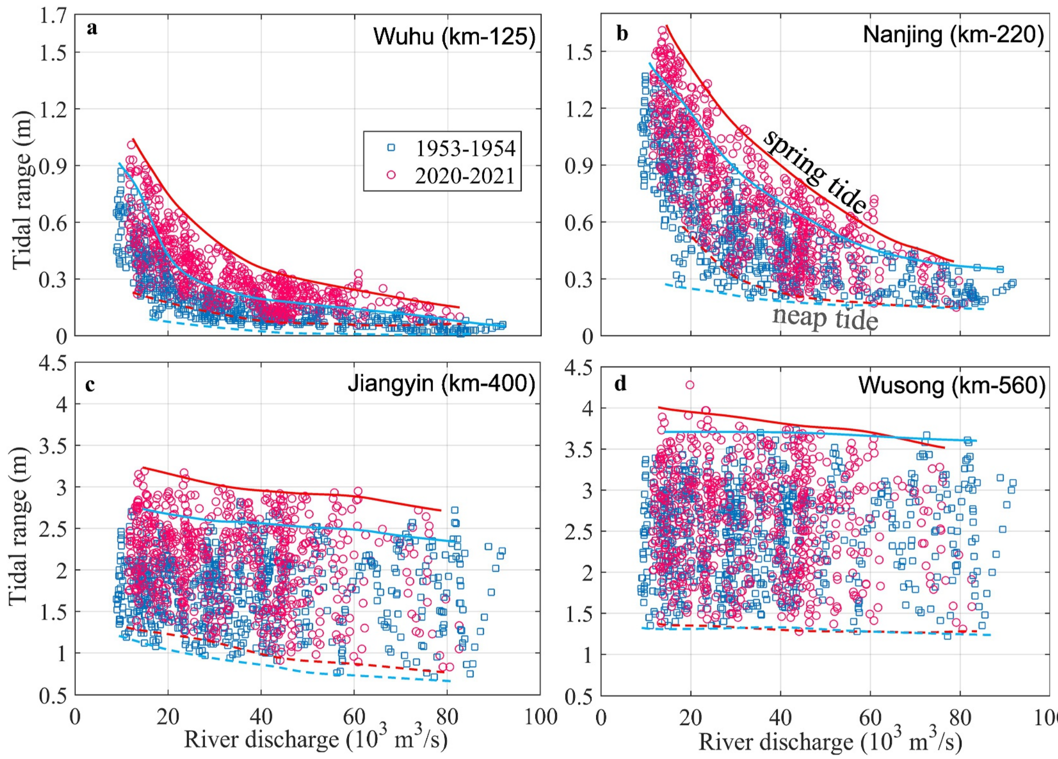

Figure 5. Changes of daily tidal ranges at gauges in the tidal river with increasing river discharge at Datong (km-0) in 1953–1954 and 2020–2021: (a) Wuhu (km-125), (b) Nanjing (km-220), (c) Jiangyin (km-400) and (d) Wusong (km-560). The solid and dashed lines indicate the envelops of spring and neap tidal ranges, respectively.

cycle, and the semi-annual tidal variations actually resulted in smaller tides in July 2020 (see Figure S6 in Supporting Information S1). The subtidal water levels and tidal ranges at Wusong, which represented oceanic tidal conditions, were nearly the same during July-September in both years (Figures 5d and 6e), despite the decadal SLR (see Figure S4 in Supporting Information S1). However, spring tidal ranges within the estuary were consistently larger during the 2020 flood, particularly along the tidal river, for example, 0.24 m, 0.14 m, and 0.13 m larger at Zhenjiang, Nanjing, and Ma'anshan, respectively, compared to 1954 (Figures 5 and 6a). These larger tidal ranges explain the higher PWLs in 2020 than in 1954.

Larger tidal ranges in 2020 can occur due to smaller river flow and/or long-term tidal changes within the estuary. The peak river discharge at Datong was indeed smaller during the floods in 2020 than in 1954 (Figure 6c). To discern the impact of decadal tidal changes, we further compared data from June to August in 1953 and 2021, which were two periods with the same river discharge of 45,000 m^3/s at Datong (Figure 6d). The results show that the tidal ranges were still 0.2–0.4 m larger in 2021 than in 1953 in the tidal river (Figure 6b), while both the tidal ranges and the mean water levels at the seaward gauge Wusong were similar (Figure 6f). This comparison clearly confirms that long-term tidal changes within the delta contribute to larger tidal ranges and consequently higher PWLs during the recent 2020 flood.

Morphological changes in the river have altered the channel conveyance and this has increased the tidal range in recent years. The main Yangtze River downstream of the TGD has undergone severe bank erosion and bed scour in response to a 75%–90% decline in sediment load following TGD operation since the early 2000s (Liu et al., 2022). The cross-sectionally averaged bed levels in the downstream river have indeed dropped by 1–3 m on average, with strong erosion and a water level drop in the first 800 km of river below the TGD (Yang et al., 2023). This induced subsequently lower river stages under the same river discharge, compared to pre-TGD conditions. Channel incision migrated in the downstream direction and erosion has emerged in the tidal river (Zheng et al., 2018) and in the tidal estuary (Zhao et al., 2018) in the recent decade. As a result, river stages at Datong were 0.13 m lower in 2020 compared to 1954 under the same high river discharge of 82,000 m^3/s. This implies a decline in longitudinal surface gradient from 29.0 mm/km to 28.4 mm/km. Long-term sea-level rise further reduces this

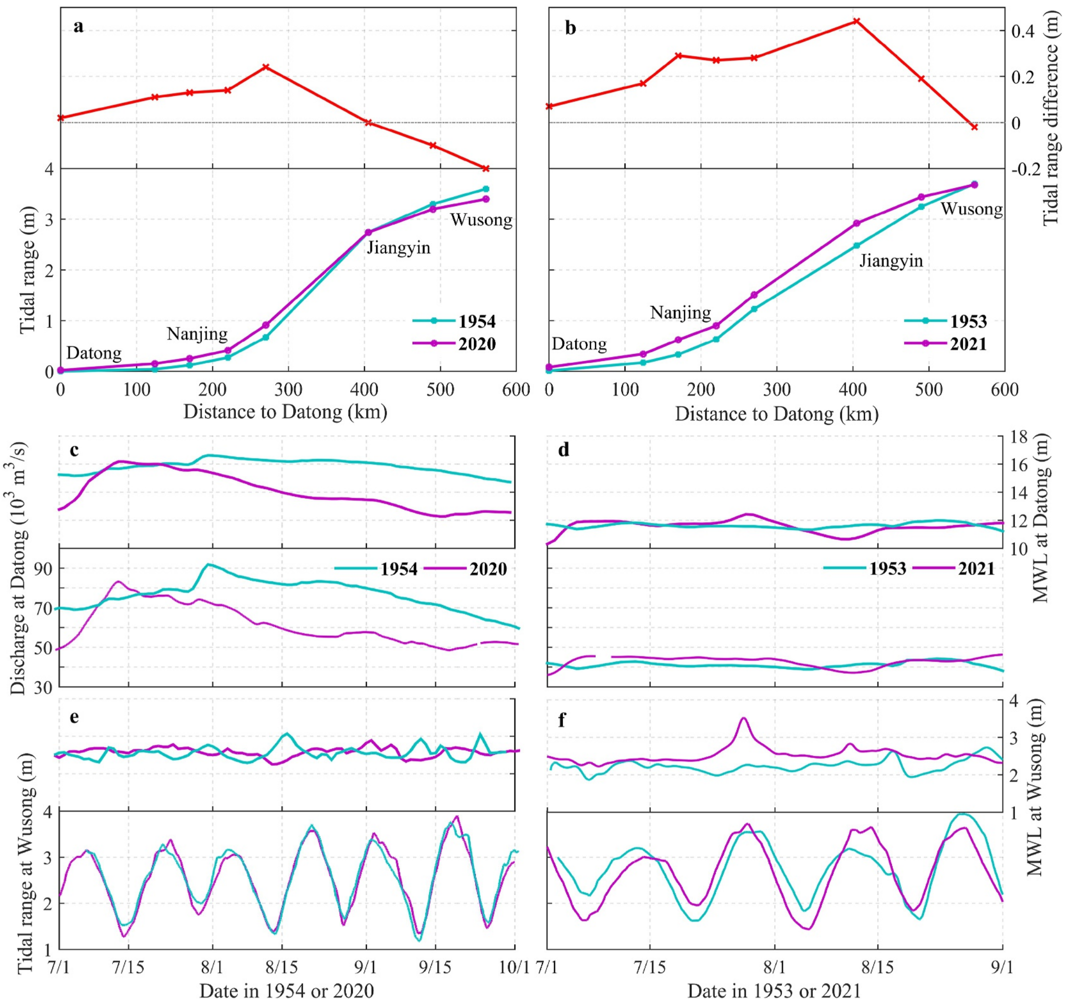

Figure 6. Comparison of river discharges, tidal ranges, and mean water levels in the Yangtze Estuary during the wet seasons between 1954 and 2020 (left panels) and between 1953 and 2021 (right panels). (a and b) Longitudinal variations of spring tidal ranges and their differences downstream of Datong. (c and d) Temporal changes of MWL and river discharge at Datong. (e and f) MWL and tidal ranges at Wusong.

longitudinal hydraulic gradient. Given that pressure gradient plays a crucial role in tidal wave dynamics (Cai et al., 2016; Kästner et al., 2019), a reduced surface gradient facilitates landward tidal wave propagation and smaller tidal damping rates, leading to larger tides in recent years than 70 years ago (Figure 5). These analyses combined demonstrate the impact of long-term sediment decline and river channel incision on mitigating tidal damping, explaining the subsequently higher PWLs and augmented flood risk in the tidal Yangtze River.

Another factor influencing the recent flood extent is the TGD operation, which has undertaken water storage-release since 2003. The TGD creates a reservoir with a flood storage capacity of 22.15 billion m^3, designed to mitigate downstream flood risk by impeding high river discharges generated in the upper river basin. The TGD outflows were indeed 18,000 m^3/s lower on July 13 and 28,000 m^3/s lower on 18 July 2020, compared to inflows, resulting in a mean reduction of 16,000 m^3/s during July 11–19 (Zhang et al., 2022). Considering a 3–5 day time lag, it is likely that the peak flood discharge occurring on 14 July 2020 at Datong could have been much larger than 84,500 m^3/s, if the TGD had not been operational. In other words, this implies that optimized real-time operation of TGD, involving reduction and delayed release of high river discharge, can help to prevent the occurrence of peak flow during spring tides and mitigate compound flood risks in the delta.

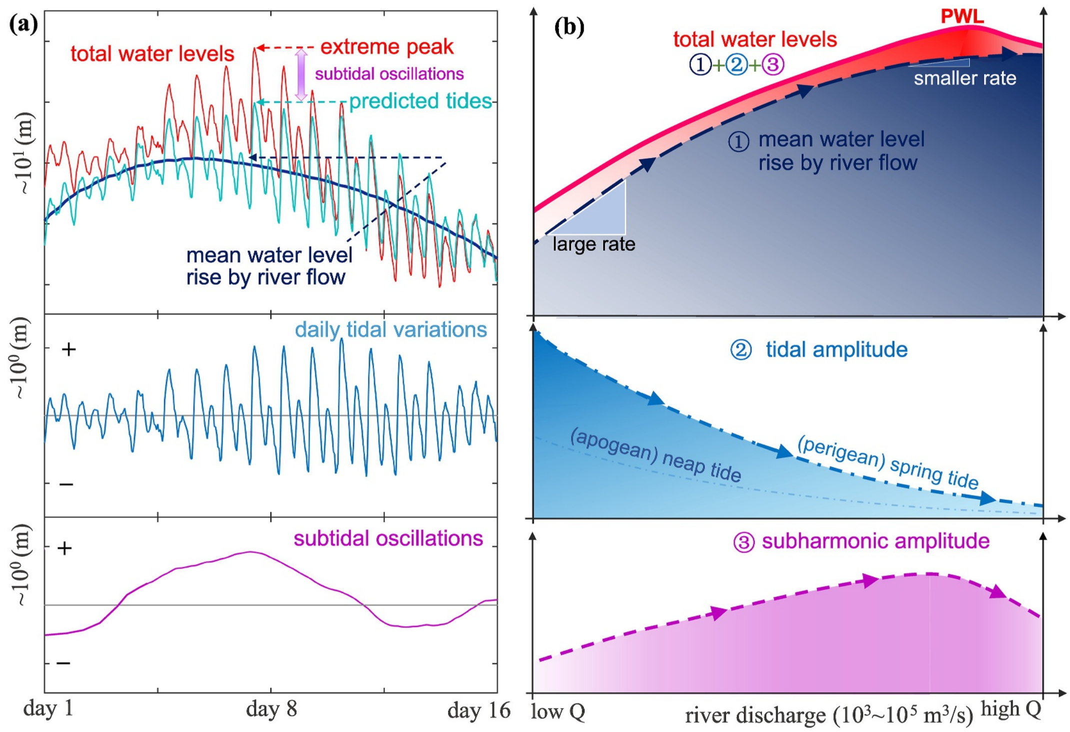

Figure 7. Conceptual illustrations of nonlinearity in total water level variations and drivers of Peak water levels (PWLs) under intermediate river discharge in tidal rivers. (a) Temporal changes of total water levels at the fortnightly time scales, including the contribution of mean water level rise by river flow, astronomical tides, and subtidal oscillations, with the extreme peak identified, highlighting the significance of subharmonics. (b) Nonlinear variations of mean water levels, tidal ranges, and subharmonic amplitudes in response to increasing river discharges. The compound effects of river, tide, and subharmonic contributions lead to the occurrence of PWLs under intermediate river discharge rather than peak discharge.

4. Discussion

4.1. Tidal River Flooding

The abovementioned data analyses revealed that the occurrence of PWLs and associated flood risk were distinct in tidal rivers from fluvial rivers and open coasts. This is because tidal rivers are exposed to strong nonlinear river-tide interactions, which result in modulation of mean water levels, tidal ranges, and reinforced local generation of subharmonics. Although river discharge and tides are the primary controls on total water levels, the culmination of astronomical tides and subharmonics at times of intermediate river discharge following peak flows are the result of non-linear river-tide interactions.

We identify three mechanisms controlling PWLs in tidal rivers. One is the delicate balance and tradeoff between river-induced subtidal water level rise and river-enhanced reduction in tidal range. Although both effects become marginal under higher river discharges (see Figures 3 and 5), higher peak river discharges damp the astronomical tides and reduce the amplitude of the diurnal and semidiurnal constituents (Figure 4b) more than they can enhance the subtidal water level rise, compared with a slightly smaller, intermediate river discharge. As a result, the combined height of subtidal levels and tidal ranges is not necessarily the largest for the peak flow (Figures 4d and 7).

The second important yet less recognized impact on the timing of PWLs regards river stage-discharge hysteresis. During the falling limb of a river discharge hydrograph, river stage is higher compared to the rising limb under the same river flow, which is generally attributed to the time lag effect in river flow flushing in river hydraulics. A similar effect applies to estuarine environments, such as in the Mahakam Estuary (Sassi & Hoitink, 2013) and in the tidal Yangtze River in this study (see Figure 3). There exists a hysteresis in the subtidal water level response to a river flood wave. In the Yangtze case, the subtidal water levels at Nanjing were 0.3–0.5 m higher during the falling limb of river discharge than that during the rising limb under the same high river discharge of 80,000 m^3/s

(see Figure 3a). This lag effect favors formation of higher subtidal water levels and PWLs during the post-peak flow periods.

The third significant mechanism lies in the modulating effect of subharmonics, by elevating subtidal water levels and subsequently PWLs during perigean spring tides, when tidal ranges are coherently larger. Both data analysis and modeling results demonstrate that the river discharge favors the generation of the MSf constituent (Figure 4c and Figure S2 in Supporting Information S1), due to river-enhanced subtidal friction, in comparison with the well-acknowledged role of river discharge in dissipating astronomical tides. Data analysis clearly shows that the MSf constituent is small in the coastal ocean, but gains energy inside the estuary (Figure 4c). A larger river discharge leads to larger MSf amplitudes throughout the Yangtze Estuary (Figure 4c). Model results also confirm that the subharmonics are indeed generated locally inside the estuary. Noises or sources originating from non-stationary river discharge and/or marine forcing play a minor role, since a stationary river discharge and only astronomical tides are prescribed as boundary conditions (Figure S2 in Supporting Information S1). The model results also show that increased river discharge leads to an increase in MSf and Mm amplitudes until they reaches a peak under intermediate flow conditions.

Regarding the optimal conditions for subharmonics, Guo et al. (2020) employed a similar schematized model to explore river-tide interactions and found that MSf amplitudes tend to be maximal when the river discharge to tidal discharge ratio is close to a unity. Similarly, Elahi et al. (2020) reported a velocity ratio of river flow and tidal flow of one to be the optimal condition for M_4 overtide generation, based on data in the Ganges Delta. These findings suggest a parameterization of the intermediate river discharge when subharmonics culminate, that is, a dynamic balance between river and tidal forcing.

Nonlinear river-tide interactions are physically attributed to the two-fold impact of river flow in enhancing both astronomical tidal energy dissipation and nonlinear energy transfer from astronomical diel bands to subharmonics (Elahi et al., 2020; Sassi & Hoitink, 2013). Consequently, subharmonics like MSf and Mm tend to be largest under an intermediate river discharge, rather than at a peak discharge that dissipates the incoming tides too much, and constrains the energy transfer to local subharmonics (Figure 7). This partly explains why the subharmonic-amplified PWLs do not occur during peak flow conditions.

PWLs in inland tidal rivers are particularly subject to the influence of subharmonics because of their low-frequency and long-wave nature. The fortnightly MSf constituent is small in amplitude and negligible in the coastal oceans compared with astronomical constituents (see Figure 4c; LeBlond, 1979; Guo et al., 2020). They intensify within estuaries and deltas, and become significant in tidal rivers where astronomical tides have largely been dissipated (see Figure S2 in Supporting Information S1). For instance, the MSf amplitude increased from less than 0.03 m at Shenshan, the sea gauge, to 0.30 m at the tidal river gauge in Zhenjiang (Figure 4c). The wave length of subharmonics is likely to be much longer than the physical length of any estuary on earth, for example, subtidal wave length about 10 times the estuary length in a ∼175 km long subtropical estuary (Henrie & Valle-Levinson, 2014). This highlights why tidal rivers are exposed to and susceptible to the influence of subtidal oscillations (Figure 8), and it implies that marine tidal influences can reach far upstream, well beyond the limit of astronomical tides, which in turn is already far beyond the limit of saltwater intrusion in estuaries.

4.2. Global Relevance and Implications

Compound flooding, due to the processes outlined above, is a feature of tidal rivers and is expected to be found in major estuaries and deltas around the world (Figure 9). To explore this further, we identified the tidal river length in a range of estuary and delta systems with high river flow (maximal river flow 600–270,000 m^3/s) and strong tides (spring tidal range 1.6–14 m, Table 4), based on the tidal river definition presented in the introduction. The tidal rivers range from 30 to 600 km in length, which comprise two-thirds of the total distance of tidal wave propagation in the rivers examined (Figure 10), highlighting their relevance in flood management. The data for the 30 systems examined suggests that tidal river length scales with both the length of tidal influence (Figure 10c) and river discharge (Figure 10b). The river-to-ocean transitional channel length is much larger in these large rivers with larger river discharge, for example, the Amazon and Yangtze rivers. Seemingly at odds with the role of river discharge in damping and retarding astronomical tidal propagation, this is likely explained by the high convergence of cross-sectional area from a wide entrance in these long systems. Overall, we see that the cumulative length of the 30 identified global tidal rivers is over 3,380 km (Table 4), implying shorelines cumulatively longer than 6,760 km that are potentially vulnerable to tidal river flood extremes.

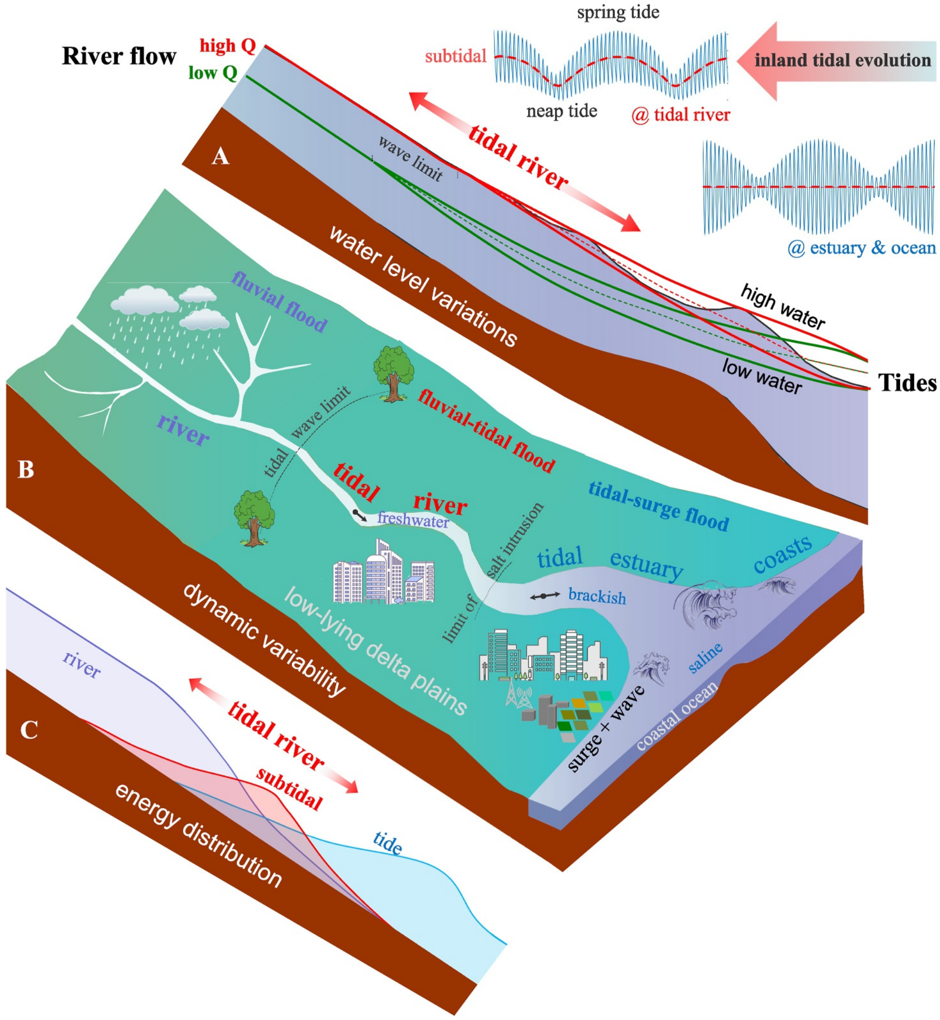

Figure 8. Schematic illustrations depicting spatial variations in river influence, tidal signals, energy distributions, and flood risk in the river-to-coast continuum, highlighting the distinct dynamics in the tidal river reaches. (a) A side view of the longitudinal profile displaying the low water and high water envelopes and their adaptation under high and low river discharges (Q), with distinct temporal tidal water level variations between the estuary and the tidal river. (b) Three-dimensional representation showing spatially varying flood drivers, including fluvial flooding in rivers, fluvial-tidal compound flooding along tidal rivers, and tidal-surge-wave compound flooding in tidal estuaries and open coastal zones. (c) A side view of streamwise distribution of fluvial and marine forcing energy, serving as indicators of flood source dominance along the river-delta-coast continuum.

The tidal rivers examined all exhibit significant subharmonics, with MSf amplitude ranging from 0.09 to 0.65 m (Elahi et al., 2020; Gallo & Vinzon, 2005; Jay & Naik, 2011; Losada et al., 2017; Luo et al., 2020; Sassi & Hoitink, 2013; Wolanski et al., 1997), confirming the global prevalence of subtidal oscillations (Table 4). For instance, LeBlond (1979) observed prominent oscillations in subtidal water levels in the upper St. Lawrence Estuary, due to a forced fortnightly tide 0.3 m in amplitude (Matte et al., 2018). Tidal height data in the Mahakam Delta show consistently higher subtidal water levels during spring tides than neap tides, with a difference up to 0.4 m (Sassi & Hoitink, 2013). The MSf amplitude is up to 0.2 m both in the Columbia Estuary (Jay et al., 2016) and the tidal rivers of the Pearl River Delta (Luo et al., 2020). Moreover, data analyses and model results show that the MSf amplitude is larger in the Amazon Delta and Ganges-Brahmaputra-Meghna Delta under larger river discharge than small discharge conditions (Elahi et al., 2020; Gallo & Vinzon, 2005), which is consistent with the results in the Yangtze (see Figure 4c). Furthermore, based on the assembled data from 30 global estuaries and deltas, we also see that the MSf amplitude is larger in these large rivers with larger river discharge magnitude (Figure 10a), confirming the role of river discharge in stimulating subharmonic generation. Similarly, the

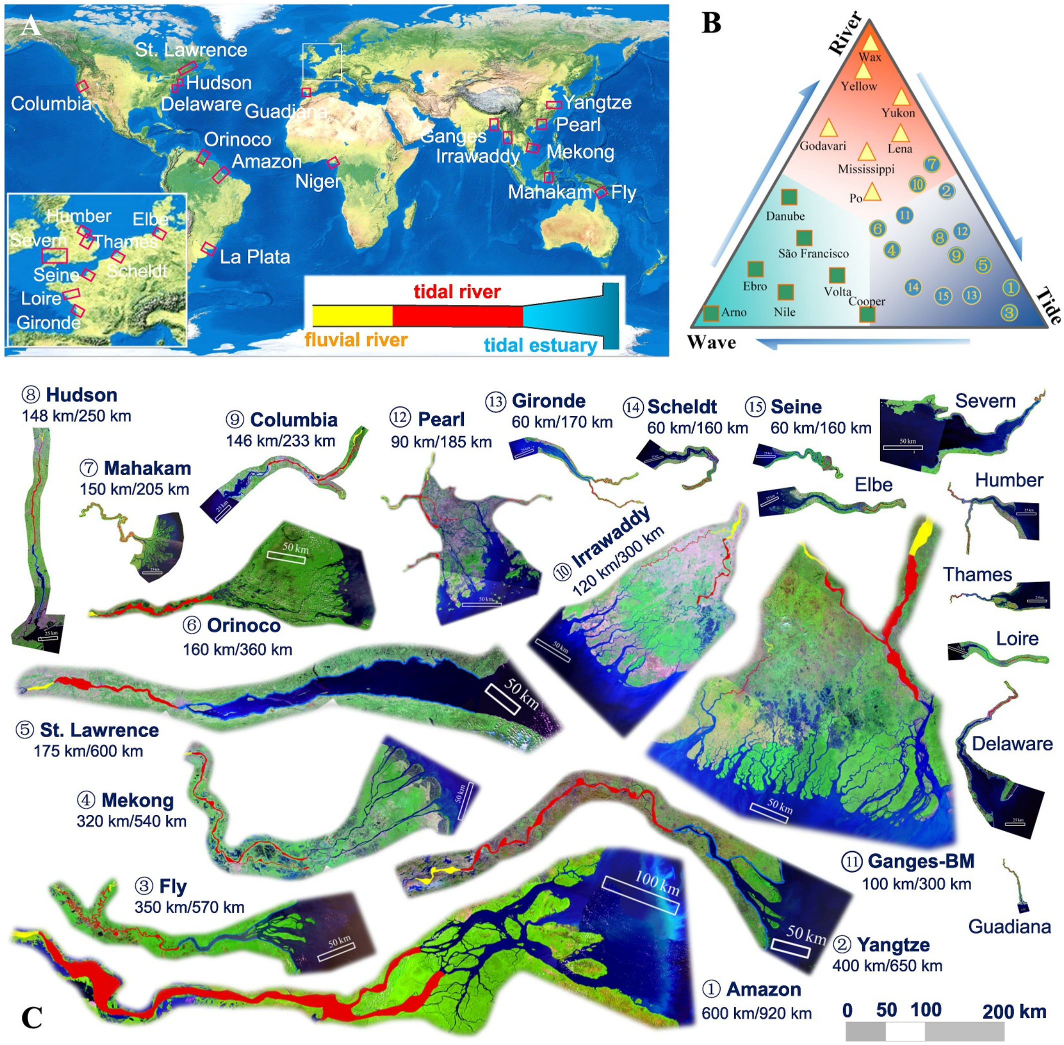

Figure 9. A synthesis of global large rivers featuring lengthy tidal rivers. (a) Global distribution of the identified rivers and deltas. (b) Classification of the identified estuaries and deltas in the river-tide-wave ternary framework. (c) Satellite imagery displaying delineated segments of tidal rivers (highlighted in red). All satellite images are obtained from Landsat 8 (USGS) and are presented at the same spatial scale. The numerical values appended to river names indicate the length of tidal river reaches relative to the maximal distance of inland tidal propagation. Deltas dominated by river and/or waves, with negligible tidal impact, such as the Mississippi, Nile, and Danube Deltas, are excluded due to limited tidal impact on water levels and flood risk within the deltaic channels. The location of the deltas in the river-tide-wave ternary diagram (panel B) is based on the relative magnitude of river discharge, tidal range, and mean wave height, according to the initial framework of Galloway (1975). The estuaries and deltas in panel (c) are listed as numbered in Table 4, according to the tidal river length.

amplitude of monthly Mm tide is in the range of 0.03–0.73 in coastal oceans and estuaries like the Amazon and Yangtze (Crawford, 1982; Gallo & Vinzon, 2005; Guo et al., 2015), though it is much less studied and documented compared with MSf due to its lower frequency. With such profound amplitudes, the MSf and Mm tides are expected to elevate high waters during perigean spring tides and enhance the consequent flood risk. Note that the identified MSf and Mm amplitudes are comparable to the extent of centennial sea-level rise; thus, overlooking the impact of subharmonics may substantially underestimate flood risk and hazards (Jiang et al., 2024; Ward et al., 2015).

Similar flood events indeed have occurred in the large estuaries like the Mekong and Amazon, although the compound effects were not explicitly identified. Specifically, water level data during the flood season in 2011 throughout the Mekong Delta illustrated the occurrence of PWLs in the river-tide transition reaches at the end of

Table 4
Global River Deltas Identified With Significant Tidal River Length and Significant Subtidal Amplitudes

No.	River name	Max river discharge (m^3/s)	Max tidal range (m)	MSf amplitude (m)	Max distance of tidal influence (km)	Length of tidal river (km)	References
1	Amazon	270,000	6.0	0.25	920	600	Gallo and Vinzon (2005)
2	Yangtze	92,600	5.9	0.38	650	400	Guo et al. (2015) and this study
3	Fly	7,500	5.0	0.20	570	350	Wolanski et al. (1997)
4	Mekong	40,000	3.5	–	540	320	Gugliotta et al. (2017)
5	St. Lawrence	32,700	7.0	0.30	600	175	Godin (1999) and Matte et al. (2018)
6	Qiantang	15,000	9.0	0.65	300	170	H. Zhou et al. (2024)
7	Orinoco	81,000	2.6	–	360	160	Warne et al. (2002)
8	Mahakam	5,000	3.0	0.12	205	150	Sassi et al. (2012)
9	Hudson	6,000	1.6	0.06	250	148	Geyer and Chant (2006)
10	Columbia	39,000	3.8	0.20	233	146	Jay et al. (2015)
11	Irrawaddy	40,400	6.4	–	300	120	Hedley et al. (2010)
12	Ganges-BM	80,000	6.0	0.50	300	100	Elahi et al. (2020)
13	Pearl	10,200	3.4	0.20	185	90	Luo et al. (2020) and Chen and Zhang (2020)
14	Gironde	5,000	6.0	–	170	60	Jalón-Rojas et al. (2015, 2018)
15	Scheldt	600	6.0	–	160	60	Horrevoets et al. (2004) and Van Rijn (2011)
16	Seine	2,300	8.0	–	160	60	Guézennec et al. (1999) and Lesourd et al. (2001)
17	Guadiana	2,500	3.6	0.10	78	55	Garel and Cai (2018)
18	Delaware	5,000	2.7	–	215	50	Cook et al. (2007)
19	Humber	1,500	7.2	–	147	45	Van Rijn (2011)
20	Elbe	3,600	3.8	–	140	35	Winterwerp et al. (2013)
21	Loire	4,500	5.5	0.24	100	30	George and Simon (1984) and Jalón-Rojas et al. (2016)
22	Severn	1,210	14.0	0.16	185	30	Liang et al. (2014)
23	Thames	700	6.6	–	110	30	Uncles and Mitchell (2011) and Primier et al. (2019)
24	La Plata	90,000	1.0	–	385	#	Dinápoli et al. (2020)
25	Gongo	80,000	1.9	–	140	#	Bars et al. (2016)
26	Niger	27,600	1.9	–	260	#	Musa et al. (2016)
27	Red	33,600	3.6	–	180	#	Pruszak et al. (2005)
28	Fraser	17,000	5.0	0.09	110	#	Wu et al. (2022)
29	Sacramento	13,800	1.8	0.10	200	#	Szlemp (2020) and Baranes et al. (2023)
30	Guadalquivir	6,000	3.5	0.11	110	#	Losada et al. (2017)

Note. Inland tidal propagation is constrained by dams or weirs in the lower Columbia, Elbe, Humber, and Hudson River. (#) indicates that the tidal river length is unknown.

October, which were nearly one month later compared with the peak discharge (see Figure 3 in Gugliotta et al. [2017]). Higher subtidal water levels during the perigean spring tide in late October exactly explained the time lag. This is consistent with the findings regarding the PWL timing in the Yangtze.

In the macro-tidal Amazon Delta, the amplitudes of MSf and Mm tides were up to be 0.25 and 0.73 m, respectively (Fassoni-Andrade et al., 2023; Gallo & Vinzon, 2005). The MSf to M_2 amplitude ratio reached two in the tidal river, leading to 0.2–0.5 m higher high water levels at spring tides than at neap tides (Fassoni-Andrade et al., 2023). The yearly maximum water levels in the tidal Amazon river occurred during the spring tides in the rainy season with a high river discharge (during late April and early May), when the subtidal signals were significant. The low-frequency subtidal signals appeared to "dictate the occurrence of the total water level max"

10.1029/2025AV002247

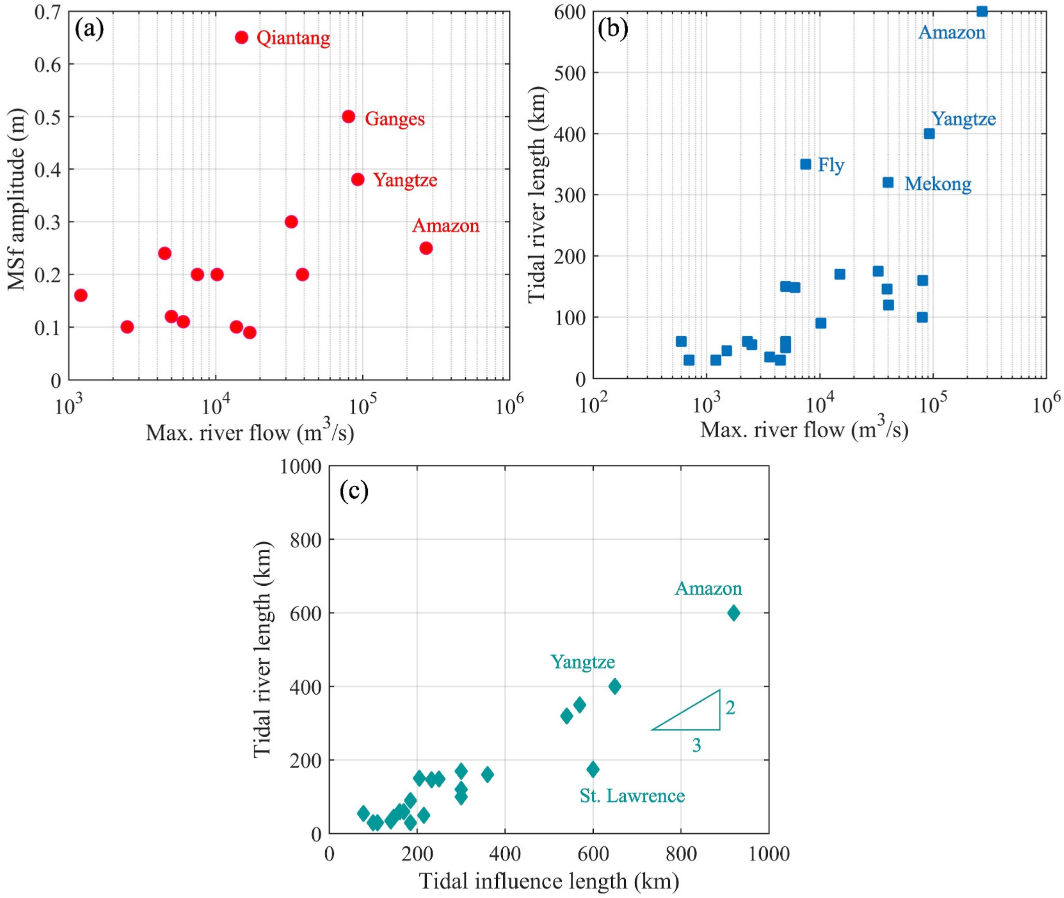

Figure 10. Variations of (a) MSf amplitude and (b) tidal river length with changes in maximal river discharge, and (c) variations of tidal river length with tidal influence length, based on data from the globally identified 30 estuaries and deltas. See Table 4 for the systems.

(Coulet et al., 2025b). In particular, the fortnightly and monthly signals combined contributed to the yearly maximal water levels during the extreme floods in 2021, by an extra elevation up to 0.40 m, which was even larger than the local M_2 amplitude (Coulet et al., 2025a). These data and observations in the Mekong and Amazon Deltas further highlight the significance of subharmonics in modulating the timing and magnitude of PWLs.

The role of subharmonics in elevating subtidal water levels and possibly PWLs during perigean spring tides is likely ubiquitous in estuaries worldwide, although the optimal threshold for subharmonic generation may not be reached for many small rivers and estuaries due to relatively small river discharge (determined by watershed area and precipitation) compared with a large tidal discharge. This explains why nonlinear river-tide interactions and consequent impact on PWLs are more significant and so far more often detected in large estuaries like the Amazon, the Mekong, and the Yangtze.

Finally, tidal river flooding is likely to escalate in future due to sea-level rise and intensified human interventions globally. Sea-level rise induces larger channel depth and a reduction in friction, likely causing a landward extension of tidal influence, larger tides and higher PWLs due to subsequent changes in tidal oscillations (Devlin et al., 2017). Sea-level rise also yields a higher oceanic base, amplifies the backwater effect on the river outflow and attenuates the streamwise pressure gradient essential for transporting fluvial water to the oceans, possibly further exacerbating compound flood events in estuaries (Moftakhari et al., 2017). On the time scales of decades to centuries, human activities such as intertidal flat reclamation and channel dredging have modified estuarine and deltaic morphology to a profound degree, resulting in amplified tides, more inland tidal influences, and heightened PWLs in many estuaries and deltas worldwide (Talke & Jay, 2020; van Maren et al., 2025; Winterwerp et al., 2013). For instance, the 100-year flood magnitude has increased over the past century in the lower

Mississippi River, with the impact of river engineering (e.g., artificial levees) outpacing climate change (Munoz et al., 2018). The maximal tidal range has increased by 1 m over 100 years (1900–2000), with a location that has moved upstream by more than 20 km in the western Scheldt Estuary, due to the feedback impact of channel deepening and reclamation of intertidal area (Wang et al., 2019). Sand mining and dredging in the Pearl Delta have induced larger channel depth and enhanced river-tide interactions, resulting in surprisingly higher PWLs (Bao et al., 2022). These qualitative observations suggest that long-term changes in tidal evolution and concomitant adaptation to sea-level rise, river morphology, and engineering tend to amplify PWLs, demonstrating an urgent need to adapt to a likely increasing fluvial-tidal compound flood risk in global tidal rivers and estuaries.

5. Conclusions

Analysis of two historical flood events in the tidal Yangtze River leads to the insight that in tidal rivers, PWLs are likely to occur during the perigean spring tide after peak flow rather than during the peak of the river flood wave. River discharge attenuates astronomical diurnal and semidiurnal tides and stimulates local generation of subharmonic (fortnightly and monthly) oscillations; the latter elevate subtidal water levels during perigean spring tides. Fluvial hysteresis in the river stage-discharge relation persists in tidal rivers, inducing higher water levels during the falling limb of discharge hydrograph. These impacts combined explain why daily PWLs in tidal rivers are likely to occur during perigean spring tide after rather than before the peak flow.

Tidal river PWLs are expected to escalate in many systems due to sediment depletion, channel deepening and sea-level rise, which amplify the tidal motion. Especially channel deepening explains the record-breaking PWLs during the recent 2020 flood in the tidal Yangtze River, which occurred under a smaller peak river discharge than during the 1954 flood. Complex river discharge-tide interactions have unanticipated implications for early flood warning, and a call for identification of a critical time window of opportunity for evacuation and flood mitigation along tidal rivers. A brief review of 30 tidal rivers worldwide underscores the need to incorporate subharmonic tidal dynamics into continental and global flood mapping, and to provide a shared knowledge base for hydrologists, coastal oceanographers, and decision-makers.

Conflict of Interest

The authors declare no conflicts of interest relevant to this study.

Availability Statement

All data needed to evaluate the conclusions are present in the paper and the Supplementary Materials. Specifically, tidal data during both floods are from open sources (www.cjh.com.cn; www.jsswj.com.cn) and are available on https://doi.org/10.6084/m9.figshare.32048682.

Acknowledgments
This work is financially supported by the Natural Science Foundation of China (Nos. U24A20181; 42476162; 42376168; 42476215; 42206169). We extend our appreciation to Prof. Amir AghaKouchak (University of California Irvine) and Prof. Wu Hui (East China Normal University) for their comments during the conceptual development.

References

Aubrey, D. G., & Speer, P. E. (1985). A study of non-linear tidal propagation in shallow inlet/estuarine systems. Part I: Observations. *Estuarine, Coastal and Shelf Science*, *21*(2), 185–205. https://doi.org/10.1016/0272-7714(85)90096-4
Balica, S. F., Wright, N. G., & van der Meulen, F. (2012). A flood vulnerability index for coastal cities and its use in assessing climate change impact. *Natural Hazards*, *64*, 73–105.
Bao, S., Zhang, W., Qin, J., Zheng, J., Lv, H., Feng, X., et al. (2022). Peak water level response to channel deepening depends on interaction between tides and the river flow. *Journal of Geophysical Research: Oceans*, *127*(4), e2021JC017625. https://doi.org/10.1029/2021jc017625
Baranes, H., Talke, S. A., Dykstra, S., & Jay, D. A. (2023). Sea level rise and variability in the Sacramento-San Joaquin Delta. *Scientific Reports*, *13*(1), 22454. https://doi.org/10.1038/s41598-023-49204-z
Bars, Y. L., Vallaeys, Y., Deleersnijder, E., Hanert, E., Carrere, L., & Channelière, C. (2016). Unstructured-mesh modeling of Congo river-to-sea continuum. *Ocean Dynamics*, *66*(4), 589–603. https://doi.org/10.1007/s10236-016-0939-x
Cai, H., Savenije, H. H. G., Jiang, C., Zhao, L., & Yang, Q. (2016). Analytical approach for determining the mean water level profile in an estuary with substantial fresh water discharge. *Hydrology and Earth System Sciences*, *20*(3), 1–19. https://doi.org/10.5194/hess-20-1177-2016
Chen, J., & Zhang, W. (2020). Impact of tidal species on water level variations in Pearl River Delta channel networks. *Regional Studies in Marine Science*, *35*, 101110. https://doi.org/10.1016/j.rsma.2020.101110
Cook, T. L., Sommerfield, C. K., & Wong, K. C. (2007). Observation of tidal and springtime sediment transport in the upper Delaware Estuary. *Estuarine, Coastal and Shelf Science*, *72*(1–2), 235–246. https://doi.org/10.1016/j.ecss.2006.10.014
Coulet, P., Durand, F., Fassoni-Andrade, A., Khan, J., Testut, L., Toublanc, F., et al. (2025a). Assessment of hydrodynamic signature of the record-breaking 2021 flood along the Amazon Estuary. *Ocean Modelling*, *196*, 102536. https://doi.org/10.1016/j.ocemod.2025.102536
Coulet, P., Durand, F., Fassoni-Andrade, A., Khan, M. J. U., Testut, L., Toublanc, F., et al. (2025b). Dynamics of yearly maximum water levels in the Amazon Estuary. *Estuaries and Coasts*, *48*(2), 54. https://doi.org/10.1007/s12237-025-01483-7
Crawford, W. R. (1982). Analysis of fortnightly and monthly tides. *International Hydrographic Review*, *59*(1), 131–141.

Dalrymple, R. W., & Choi, K. (2007). Morphologic and facies trends through the fluvial-marine transition in tide-dominated depositional systems: A schematic framework for environmental and sequence-stratigraphic interpretation. *Earth-Science Reviews*, *81*(3–4), 135–174. https://doi.org/10.1016/j.earscirev.2006.10.002

Devlin, A. T., Jay, D. A., Talke, S. A., Zaron, E. D., Pan, J., & Lin, H. (2017). Coupling of sea level and tidal range changes, with implications for future water levels. *Scientific Reports*, *7*(1), 17021. https://doi.org/10.1038/s41598-017-17056-z

Dinápoli, M. G., Simionato, C. G., & Moreira, D. (2020). Nonlinear tide-surge interactions in the Rio de la Plata Estuary. *Estuarine, Coastal and Shelf Science*, *241*, 106834. https://doi.org/10.1016/j.ecss.2020.106834

Du, H., Fei, K., & Gao, L. (2024). Nonlinear tide-river-surge interactions and their impacts on compound flooding during typhoon Hato in the Pearl River Delta. *Journal of Geophysical Research: Oceans*, *129*(11), e2023JC020673. https://doi.org/10.1029/2023jc020673

Elahi, M. W. E., Jalón-Rojas, I., Wang, X. H., & Ritchie, E. A. (2020). Influence of seasonal river discharge on tidal propagation in the Ganges-Brahmaputra-Meghna Delta, Bangladesh. *Journal of Geophysical Research: Oceans*, *125*(11), e2020JC016417. https://doi.org/10.1029/2020jc016417

Fassoni-Andrade, A. C., Durand, F., Azevedo, A., Bertin, X., Santos, L. G., Khan, J. U., et al. (2023). Seasonal to interannual variability of the tides in the Amazon Estuary. *Continental Shelf Research*, *255*, 104945. https://doi.org/10.1016/j.csr.2023.104945

Gallo, M. N., & Vinzon, S. B. (2005). Generation of overtides and compound tides in the Amazon Estuary. *Ocean Dynamics*, *65*, 441–448.

Galloway, W. (1975). Process framework for describing the morphologic and stratigraphic evolution of deltaic depositional system. SEPM, Special Publication No. 31 (pp. 127–156).

Ganguli, P., & Merz, B. (2019). Trends in compound flooding in northwestern Europe during 1901–2014. *Geophysical Research Letters*, *46*(19), 10810–10820. https://doi.org/10.1029/2019gl084220

Garel, E., & Cai, H. Y. (2018). Effects of tidal-forcing variations on tidal properties along a narrow convergent estuary. *Estuaries and Coasts*, *41*(7), 1924–1942. https://doi.org/10.1007/s12237-018-0410-y

George, K. J., & Simon, B. (1984). The species concordance method of tide prediction in estuaries. *International Hydrographic Review*, *LXI*(1), 121–146.

Geyer, W. R., & Chant, R. (2006). The physical oceanography processes in the Hudson River Estuary. In J. S. Levinton & J. R. Waldman (Eds.), *The Hudson River Estuary* (pp. 1–23). Cambridge University Press.

Godin, G. (1999). The propagation of tides up rivers with special consideration of the upper Saint Lawrence River. *Estuarine, Coastal and Shelf Science*, *48*(3), 307–324. https://doi.org/10.1006/ecss.1998.0422

Grinsted, A., Moore, J. C., & Jevrejeva, S. (2004). Application of the cross wavelet transform and wavelet coherence to geophysical time series. *Nonlinear Processes in Geophysics*, *11*(5–6), 561–566.

Guézennec, L., Lafite, R., Dupont, J. P., Meyer, R., Boust, D., & Guezennec, L. (1999). Hydrodynamics of suspended particulate matter in the tidal freshwater zone of a macrotidal estuary. *Estuaries*, *22*(3A), 717–727. https://doi.org/10.2307/1353058

Gugliotta, M., & Saito, Y. (2019). Matching trends in channel width, sinuosity, and depth along the fluvial to marine transition zone of tide-dominated river deltas: The need for a revision of depositional and hydraulic models. *Earth-Science Reviews*, *191*, 93–113. https://doi.org/10.1016/j.earscirev.2019.02.002

Gugliotta, M., Saito, Y., Nguyen, V. L., Ta, T. K. O., Nakashima, R., Tamura, T., et al. (2017). Process regime, salinity, morphological, and sedimentary trends along the fluvial to marine transition zone of the mixed-energy Mekong River Delta, Vietnam. *Continental Shelf Research*, *147*, 7–26. https://doi.org/10.1016/j.csr.2017.03.001

Guo, L. (2026). Tidal height data during the floods in 1954 and 2020 in the Yangtze Estuary [Dataset]. *Figshare*. https://doi.org/10.6084/m9.figshare.32048682.v1

Guo, L., van der Wegen, M., Jay, D. A., Matte, P., Wang, Z. B., Roelvink, D., & He, Q. (2015). River-tide dynamics: Exploration of nonstationary and nonlinear tidal behavior in the Yangtze River estuary. *Journal of Geophysical Research: Oceans*, *120*(5), 3499–3521. https://doi.org/10.1002/2014jc010491

Guo, L., Zhu, C., Wu, X., Wan, Y., Jay, D. A., Townend, I., et al. (2020). Strong inland propagation of low-frequency long waves in river estuaries. *Geophysical Research Letters*, *47*(19), e2020GL089112. https://doi.org/10.1029/2020gl089112

Hedley, P. J., Bird, M. I., & Robinson, R. A. (2010). Evolution of the Irrawaddy delta region since 1850. *The Geographical Journal*, *176*(2), 138–149. https://doi.org/10.1111/j.1475-4959.2009.00346.x

Helaire, L. T., Talke, S. A., Jay, D. A., & Chang, H. (2020). Present and future flood hazard in the lower Columbia River Estuary: Changing flood hazards in the Portland-Vancouver Metropolitan area. *Journal of Geophysical Research: Oceans*, *125*(7), e2019JC015928. https://doi.org/10.1029/2019jc015928

Henrie, K., & Valle-Levinson, A. (2014). Subtidal variability in water levels inside a subtropical estuary. *Journal of Geophysical Research: Oceans*, *119*(11), 7483–7492. https://doi.org/10.1002/2014JC009829

Hoitink, A. J. F., & Jay, D. A. (2016). Tidal river dynamics: Implications for deltas. *Reviews of Geophysics*, *54*(1), 240–272. https://doi.org/10.1002/2015rg000507

Hoitink, A. J. F., Wang, Z. B., Vermeulen, B., Huismans, Y., & Kästner, K. (2017). Tidal controls on river delta morphology. *Nature Geoscience*, *10*(9), 637–645. https://doi.org/10.1038/ngeo3000

Horrevoets, A. C., Savenije, H. H. G., Schuurman, J. N., & Graas, S. (2004). The influence of river discharge on tidal damping in alluvial estuaries. *Journal of Hydrology*, *294*(4), 213–228. https://doi.org/10.1016/j.jhydrol.2004.02.012

Jalón-Rojas, I., Schmidt, S., & Sottolichio, A. (2015). Turbidity in the fluvial Gironde Estuary (southwest France) based on 10-year continuous monitoring: Sensitivity to hydrological conditions. *Hydrology and Earth System Sciences*, *19*(6), 2805–2819. https://doi.org/10.5194/hess-19-2805-2015

Jalón-Rojas, I., Schmidt, S., & Sottolichio, A. (2016). Evaluation of spectral methods for high-frequency multiannual time series in coastal transitional waters: Advantage of combined analyses. *Limnology and Oceanography: Methods*, *14*(6), 381–396. https://doi.org/10.1002/lom3.10097

Jalón-Rojas, I., Sottolichio, A., Hanquiez, V., Fort, A., & Schmidt, S. (2018). To what extent multidecadal changes in morphology and fluvial discharge impact tides in a convergent (turbid) tidal river. *Journal of Geophysical Research: Oceans*, *123*(5), 3241–3258. https://doi.org/10.1002/2017jc013466

Jay, D. A., Borde, A., & Diefenderfer, H. (2016). Tidal-fluvial and estuarine processes in the Lower Columbia River: II: Water level models, inundation, reach classification and vegetation. *Estuaries and Coasts*, *39*(5), 1299–1324. https://doi.org/10.1007/s12237-016-0082-4

Jay, D. A., Leffler, K., Difenderfer, H. L., & Borde, A. B. (2015). Tidal-fluvial and estuarine processes in the lower Columbia River: I. Along-channel water level variations, Pacific Ocean to Bonneville Dam. *Estuaries and Coasts*, *38*(2), 415–433. https://doi.org/10.1007/s12237-014-9819-0

Jay, D. A., & Naik, P. K. (2011). Distinguishing human and climate influences on hydrological disturbance processes in the Columbia River, USA. *Hydrological Sciences Journal*, *56*(7), 1186–1209. https://doi.org/10.1080/02626667.2011.604324

Jiang, S., Tarasova, L., Yu, G., & Zscheischler, J. (2024). Compounding effects in flood drivers challenge estimates of extreme river floods. *Science Advances*, *10*(13), eadl4005. https://doi.org/10.1126/sciadv.adl4005

Jongman, B., Winsemius, H. C., Aerts, J. C. J. H., Coughlan de Perez, E., van Aalst, M. K., Kron, W., & Ward, P. J. (2015). Declining vulnerability to river floods and the global benefits of adaptation. *Proceedings of the National Academy of Sciences of the United States of America*, *112*(18), E2271–E2280. https://doi.org/10.1073/pnas.1414439112

Kästner, K., Hoitink, A. J. F., Torfs, P. J. J. F., Deleersnijder, E., & Ningsih, N. (2019). Propagation of tides along a river with a sloping bed. *Journal of Fluid Mechanics*, *872*, 39–73. https://doi.org/10.1017/jfm.2019.331

LeBlond, P. H. (1979). Forced fortnightly tides in shallow rivers. *Atmosphere-Ocean*, *17*(3), 253–264. https://doi.org/10.1080/07055900.1979.9649064

Lesourd, S., Lesueur, P., Brun-Cottan, J.-C., Auffret, J. P., Poupinet, N., & Laignel, B. (2001). Morphosedimentary evolution of the macrotidal Seine Estuary subject to human impact. *Estuaries*, *24*(6B), 940–949. https://doi.org/10.2307/1353008

Liang, D. F., Xia, J. Q., Falconer, R. A., & Zhang, J. (2014). Study on tidal resonance in Severn Estuary and Bristol Channel. *Coastal Engineering Journal*, *56*(1), 1–18. https://doi.org/10.1142/S0578563414500028

Liu, X., Li, M., Chen, J., Xu, Y. J., Zhang, W., Chen, Z., et al. (2022). Natural and reservoir-induced channel changes in the Yangtze River Tidal Reach. *Journal of Hydrology*, *605*, 127398. https://doi.org/10.1016/j.jhydrol.2021.127398

Losada, M. A., Díez-Minguito, M., & Reyes-Merlo, M. Á. (2017). Tidal-fluvial interaction in the Guadalquivir River Estuary: Spatial and frequency-dependent response of currents and water levels. *Journal of Geophysical Research: Oceans*, *122*(2), 847–865. https://doi.org/10.1002/2016jc011984

Luo, X., Zhang, W., Chen, S., Feng, X., Ji, X., & Xu, Y. (2020). Evolution of reversal of the lowest low waters in a tidal river network. *Journal of Hydrology*, *585*, 124701. https://doi.org/10.1016/j.jhydrol.2020.124701

Matte, P., Jay, D. A., & Zaron, E. D. (2013). Adaptation of classical tidal harmonic analysis to nonstationary tides, with application to river tides. *Journal of Atmospheric and Oceanic Technology*, *30*(3), 569–589. https://doi.org/10.1175/JTECH-D-12-00016.1

Matte, P., Secretan, Y., & Morin, J. (2018). Reconstruction of tidal discharge in the St. Lawrence fluvial estuary: The method of cubature revisited. *Journal of Geophysical Research: Oceans*, *123*(8), 5500–5525. https://doi.org/10.1029/2018JC013834

Moftakhari, H., Munoz, D. F., Akbari Asanjan, A., AghaKouchak, A., Moradkhani, H., & Jay, D. A. (2024). Nonlinear interactions of sea-level rise and storm tide alter extreme coastal water levels: How and why? *AGU Advances*, *5*(2), e2023AV000996. https://doi.org/10.1029/2023AV000996

Moftakhari, H., Salvadori, G., AghaKouchak, A., Sanders, B. F., & Matthew, R. A. (2017). Compounding effects of sea level rise and fluvial flooding. *Proceedings of the National Academy of Sciences of the United States of America*, *114*(37), 9785–9790. https://doi.org/10.1073/pnas.1620325114

Munoz, S. E., Giosan, L., Therrell, M. D., Remo, J. W. F., Shen, Z., Sullivan, R. M., et al. (2018). Climatic control of Mississippi River flood hazard amplified by river engineering. *Nature*, *556*(7699), 95–98. https://doi.org/10.1038/nature26145

Musa, Z. N., Popescu, I., & Mynett, A. (2016). Assessing the sustainability of local resilience practices against sea level rise impacts on the lower Niger Delta. *Ocean & Coastal Management*, *130*, 221–228. https://doi.org/10.1016/j.ocecoaman.2016.06.016

Pawlowicz, R., Beardsley, B., & Lentz, S. (2002). Classical tidal harmonic analysis including error estimates in MATLAB using T_TIDE. *Computers & Geosciences*, *28*(8), 929–937. https://doi.org/10.1016/s0098-3004(02)00013-4

Primier, V., de Souza Machado, A. A., Mitchell, S., Zarfl, C., Spencer, K., & Toffolon, M. (2019). A model-based analysis of metal fate in the Thames Estuary. *Estuaries and Coasts*, *42*, 1185–1201.

Pruszak, Z., Szmytkiewicz, M., Hung, N. M., & Ninh, P. V. (2005). Coastal processes in the Red River Delta area, Vietnam. *Coastal Engineering Journal*, *44*(2), 97–126. https://doi.org/10.1142/s0578563402000469

Sassi, M. G., & Hoitink, A. J. F. (2013). River flow controls on tides and tide-mean water level profiles in a tidal freshwater river. *Journal of Geophysical Research: Oceans*, *118*(9), 4139–4151. https://doi.org/10.1002/jgrc.20297

Sassi, M. G., Hoitink, A. J. F., de Brye, B., & Deleersnijder, E. (2012). Downstream hydraulic geometry of a tidally influenced river delta. *Journal of Geophysical Research*, *117*(F4), F04022. https://doi.org/10.1029/2012JF002448

Spicer, P., Huguenard, K., Ross, L., & Rickard, L. N. (2019). High-frequency tide-surge-river interaction in estuaries: Causes and implications for coastal flooding. *Journal of Geophysical Research: Oceans*, *124*(12), 9517–9530. https://doi.org/10.1029/2019jc015466

Szlemp, E. (2020). *Analysis of the tidal range in the Sacramento San Joaquin Delta from 1857 to present*. MSc. thesis of California Polytechnic State University.

Talke, S. A., & Jay, D. A. (2020). Changing tides: The role of natural and anthropogenic factors. *Annual Review of Marine Science*, *12*(1), 121–151. https://doi.org/10.1146/annurev-marine-010419-010727

Tessler, Z. D., Vörösmarty, C. J., Grossberg, M., Gladkova, I., Aizenman, H., Syvitski, J. P. M., & Foufoula-Georgiou, E. (2015). Profiling risk and sustainability in coastal deltas of the world. *Science*, *349*(6248), 638–643. https://doi.org/10.1126/science.aab3574

Uncles, R. J., & Mitchell, S. B. (2011). Turbidity in the Thames Estuary: How turbid do we expect it to be? *Hydrobiologia*, *672*(1), 91–103. https://doi.org/10.1007/s10750-011-0757-6

United Nations Office for Disaster Risk Reduction (UNDRR). (2020). The human cost of disasters: An overview of the last 20 years (2000–2019) (pp. 1–17).

Valle-Levinson, A., Olabarrieta, M., & Heilman, L., (2020). Compound flooding in Houston-Galveston Bay during Hurricane Harvey. *Science of the Total Environment*, *747*, 141272. https://doi.org/10.1016/j.scitotenv.2020.141272

Van Maren, D. S., Schrijvershof, R. A., Beemster, J., Zhu, C., Xie, D., Zhou, Z., et al. (2025). Land reclamation impacts on tidal landscape evolution. *Review of Geophysics*, *63*(3), e2024RG000860. https://doi.org/10.1029/2024RG000860

Van Rijn, L. C. (2011). Comparison hydrodynamics and salinity of tidal estuaries: Elbe, Humber, Scheldt and Weser (Deltares Report No. 1203583-000). Retrieved from http://tide-project.eu/downloads/1203583-000-ZKS-0005-r-Comparison_Hydrodynamics_and_Salini-2.pdf

Wahl, T., Jain, S., Bender, J., Meyers, S. D., & Luther, M. E. (2015). Increasing risk of compound flooding from storm surge and rainfall for major US cities. *Nature Climate Change*, *5*(12), 1093–1097. https://doi.org/10.1038/nclimate2736

Wang, Z., Juken, H., & de Vriend, H. J. (1999). *Tidal asymmetry and residual sediment transport in estuaries*. (Report No. Z2749). WL|Hydraulic.

Wang, Z. B., Vandenbruwaene, W., Tall, M., & Winterwerp, H. (2019). Amplification and deformation of tidal wave in the Upper Scheldt Estuary. *Ocean Dynamics*, *69*(7), 829–839. https://doi.org/10.1007/s10236-019-01281-3

Ward, P. J., Jongman, B., Salmon, P., Simpson, A., Bates, P., De Groeve, T., et al. (2015). Usefulness and limitations of global flood risk models. *Nature Climate Change*, *5*(8), 712–715. https://doi.org/10.1038/nclimate2742

Warne, A. G., Meade, R. H., White, W. A., Guevara, E. H., Gibeaut, J., Smyth, R. C., et al. (2002). Regional controls on geomorphology, hydrology, and ecosystem integrity in the Orinoco Delta, Venezuela. *Geomorphology*, *44*(3–4), 273–307. https://doi.org/10.1016/s0169-555x(01)00179-9

Wei, K., Ouyang, C., Duan, H., Li, Y., Chen, M., Ma, J., et al. (2020). Reflections on the catastrophic 2020 Yangtze River basin flooding in southern China. *The Innovation*, *1*(2), 100038. https://doi.org/10.1016/j.xinn.2020.100038

Winterwerp, J. C., Wang, Z. B., van Braeckel, A., van Holland, G., & Kösters, F. (2013). Man-induced regime shifts in small estuaries–II: A comparison of rivers. *Ocean Dynamics*, *63*(11–12), 1293–1306. https://doi.org/10.1007/s10236-013-0663-8

Wolanski, E., King, B., & Galloway, D. (1997). Salinity intrusion in the Fly River Estuary, Papua New Guinea. *Journal of Coastal Research*, *13*(4), 983–994.

Wu, Y., Hannah, C., Matte, P., O'Flaherty-Sproul, M., Mo, R. P., Wang, X. Y., & MacAulay, P. (2022). Tidal propagation in the lower Fraser River, British Columbia, Canada. Estuarine. *Coastal and Shelf Science*, *264*, 107695. https://doi.org/10.1016/j.ecss.2021.107695

Xia, J., & Chen, J. (2021). A new era of flood control strategies from the perspective of managing the 2020 Yangtze River flood. *Science China Earth Sciences*, *64*, 1–9. https://doi.org/10.1007/s11430-020-9699-8

Yang, Y., Zhou, L., Zhu, L., Liu, W., & Wang, J. (2023). Impact of upstream reservoirs on geomorphic evolution in the middle and lower reaches of the Yangtze River. *Earth Surface Processes and Landforms*, *48*(3), 582–595. https://doi.org/10.1002/esp.5504

Zhang, H., Dou, Y., Ye, L., Zhang, C., Yao, H., Bao, Z., et al. (2022). Realizing the full reservoir operation potential during the 2020 Yangtze river floods. *Scientific Reports*, *12*, 2822.

Zhao, J., Guo, L. C., He, Q., Wang, Z. B., van Marne, D. S., & Wang, X. Y. (2018). An analysis on half century morphological changes in the Changjiang Estuary: Spatial variability under natural processes and human intervention. *Journal of Marine Systems*, *181*, 25–36. https://doi.org/10.1016/j.jmarsys.2018.01.007

Zheng, S. W., Xu, Y. J., Cheng, H. Q., Wang, B., & Wu, S. H. (2018). Riverbed erosion of the final 565 kilometers of the Yangtze River (Changjiang) following construction of the Three Gorges Dam. *Scientific Reports*, *8*(1), 11917. https://doi.org/10.1038/s41598-018-30441-6

Zhou, H., Pan, H., Gan, M., Zhang, G., Wang, S., & Ying, C. (2024). Study on the tidal variability related to flooding and hydroelectric operations in the Qiantang river estuary. *Estuarine, Coastal and Shelf Science*, *305*, 108845. https://doi.org/10.1016/j.ecss.2024.108845

Zhou, Z., Xie, S., & Zhang, R. (2021). Historic Yangtze flooding of 2020 tied to extreme Indian Ocean conditions. *Proceedings of the National Academy of Sciences of the United States of America*, *118*(12), e2022255118. https://doi.org/10.1073/pnas.2022255118